

Accepted Manuscript

Effect of aging on the structure and phosphate retention of Fe(III)-precipitates formed by Fe(II) oxidation in water

Anna-Caterina Senn, Ralf Kaegi, Stephan J. Hug, Janet G. Hering, Stefan Mangold, Andreas Voegelin

PII: S0016-7037(16)30742-6
DOI: <http://dx.doi.org/10.1016/j.gca.2016.12.033>
Reference: GCA 10085

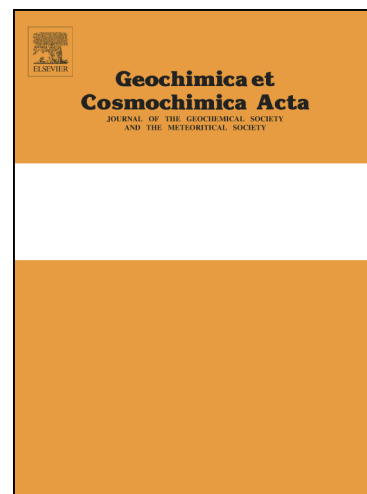
To appear in: *Geochimica et Cosmochimica Acta*

Received Date: 12 June 2016
Revised Date: 21 November 2016
Accepted Date: 22 December 2016

Please cite this article as: Senn, A-C., Kaegi, R., Hug, S.J., Hering, J.G., Mangold, S., Voegelin, A., Effect of aging on the structure and phosphate retention of Fe(III)-precipitates formed by Fe(II) oxidation in water, *Geochimica et Cosmochimica Acta* (2016), doi: <http://dx.doi.org/10.1016/j.gca.2016.12.033>

This is a PDF file of an unedited manuscript that has been accepted for publication. As a service to our customers we are providing this early version of the manuscript. The manuscript will undergo copyediting, typesetting, and review of the resulting proof before it is published in its final form. Please note that during the production process errors may be discovered which could affect the content, and all legal disclaimers that apply to the journal pertain.

This manuscript version is made available under the CC-BY-NC-ND 4.0 license
<http://creativecommons.org/licenses/by-nc-nd/4.0/>



Revised manuscript submitted for publication in *Geochimica et Cosmochimica Acta*

November 21, 2016

Effect of aging on the structure and phosphate retention of Fe(III)-precipitates formed by Fe(II) oxidation in water

*Anna-Caterina Senn^{a,b}, Ralf Kaegi^a, Stephan J. Hug^a, Janet G. Hering^{a,b,c},
Stefan Mangold^d, Andreas Voegelin^{a,*}*

^aEawag, Swiss Federal Institute of Aquatic Science and Technology, Ueberlandstrasse 133, CH-8600 Dübendorf, Switzerland

^bDepartment of Environmental Sciences, Institute of Biogeochemistry and Pollutant Dynamics, ETH, Swiss Federal Institute of Technology, Zurich, Switzerland

^cSchool of Architecture Civil and Environmental Engineering, EPFL, École Polytechnique Fédérale de Lausanne, Switzerland

^dKarlsruhe Institute of Technology, Institute of Synchrotron Radiation, Hermann-von-Helmholtz Platz 1, D-76344 Eggenstein-Leopoldshafen, Germany

* Corresponding author. E-mail address: andreas.voegelin@eawag.ch, phone +41 58 765 54 70, fax +41 58765 52 10

ABSTRACT

Iron(III)-precipitates formed by Fe(II) oxidation in aqueous solutions affect the cycling and impact of Fe and other co-precipitated elements in environmental systems. Fresh Fe(III)-precipitates are metastable and their transformation into more stable phases during aging may result in the release of initially co-precipitated ions. Phosphate, silicate, Mg and Ca play key roles in determining the structure and composition of fresh Fe(III)-precipitates. Here we examine how these ions affect the structure and phosphate retention of Fe(III)-precipitates formed by oxidation of 0.5 mM dissolved Fe(II) at pH 7.0 after aging for 30 days at 40 °C.

Iron K-edge X-ray absorption spectroscopy (XAS) shows that aged precipitates consist of the same structural units as fresh precipitates: Amorphous Fe(III)- or Ca-Fe(III)-phosphate, ferrihydrite, and poorly crystalline lepidocrocite. Mg, Ca, and dissolved phosphate stabilize (Ca-)Fe(III)-phosphate against transformation into ferrihydrite. Silicate further attenuates (Ca-)Fe(III)-phosphate transformation. The crystallinity of lepidocrocite formed in phosphate- and silicate-free solutions slightly increases during aging. The transformation of Fe(III)- and Ca-Fe(III)-phosphate into ferrihydrite and ongoing ferrihydrite crystallization during aging results in the release of co-precipitated phosphate. Dissolved Ca on the other hand limits phosphate concentrations to values consistent with the formation of octacalciumphosphate. Owing to the combined effects of Ca and silicate, phosphate is most effectively retained by Fe(III)-precipitates formed and aged in Ca- and silicate-containing solutions. The results from this study contribute to an improved understanding of the formation and transformation of Fe(III)-precipitates and emphasize that the complexity of Fe(III)-precipitate dynamics in the presence of multiple interfering solutes must be considered when addressing their impact on major and trace elements in environmental systems.

1. INTRODUCTION

The oxidation of dissolved ferrous iron in aqueous solutions leads to the formation of amorphous to poorly crystalline ferric Fe(III)-precipitates with a very high sorption capacity for a wide range of major and trace elements. Iron oxidation and precipitation occur ubiquitously in natural and engineered systems and critically affect the biogeochemical cycling of Fe and other elements, including contaminants and nutrients (Stumm and Sulzberger, 1992; Borch et al., 2010; Taylor and Konhauser, 2011; Senn et al., 2015). Phosphate uptake by Fe(III)-precipitates, for example, has been extensively studied with respect to phosphate dynamics in eutrophic aquatic systems or phosphate removal in wastewater treatment (Tessenow, 1974; Buffle et al., 1989; Frossard et al., 1997; Mayer and Jarrell, 2000; Gunnars et al., 2002; Griffioen, 2006; Mao et al., 2012; Baken et al., 2015; Baken et al., 2016). Freshly formed Fe(III)-precipitates are metastable and may transform into thermodynamically more stable phases over time, potentially resulting in the release of initially co-precipitated elements such as P or As (Fuller et al., 1993b; Mayer and Jarrell, 2000)

Among the common inorganic solutes in near-neutral freshwaters, phosphate, silicate and Ca play key roles in determining the structure and composition of fresh Fe(III)-precipitates (Buffle et al., 1989; Rose et al., 1996; Doelsch et al., 2000; Gunnars et al., 2002; Kaegi et al., 2010; Voegelin et al., 2010; Cismasu et al., 2014; van Genuchten et al., 2014a; van Genuchten et al., 2014b; Senn et al., 2015). In phosphate-containing solutions, Fe(II) oxidation leads to the formation of amorphous Fe(III)-phosphate (Tessenow, 1974; Châtellier et al., 2013; Voegelin et al., 2013). The presence of Ca in addition to phosphate leads to the precipitation of amorphous Ca-Fe(III)-phosphate with enhanced degree of Fe(III)-polymerization and higher phosphate uptake capacity compared to Ca-free Fe(III)-phosphate, due to the formation of Ca-Fe(III)-phosphate and Ca-phosphate polymers in addition to Fe(III)-phosphate polymers (Senn et al.,

2015). (Note: in this manuscript, we use the term Fe(III)-phosphate explicitly for Ca-free Fe(III)-phosphate, the term Ca-Fe(III)-phosphate for Ca-containing Fe(III)-phosphate, and the term (Ca-)Fe(III)-phosphate to refer to both.) In phosphate-free solutions, poorly crystalline lepidocrocite forms in the absence of silicate, and silicate-containing ferrihydrite-type precipitates at sufficiently high silicate concentrations (Schwertmann et al., 1984; Voegelin et al., 2010; van Genuchten et al., 2014b; Senn et al., 2015). At initial dissolved P/Fe ratios below a critical threshold, the initial formation of amorphous (Ca-)Fe(III)-phosphate leads to the depletion of dissolved phosphate and the subsequent formation of poorly crystalline lepidocrocite or a ferrihydrite-type Fe(III)-precipitate, depending on the dissolved silicate/Fe(II) ratio (Voegelin et al., 2010; van der Grift et al., 2016).

The aging of amorphous (Ca-)Fe(III)-phosphate may lead to its transformation into crystalline (Ca)-Fe(III)-phosphates, as observed for amorphous Fe(III)-arsenate and Ca-Fe(III)-arsenate (Paktunc et al., 2008; Paktunc et al., 2015). Continuing Fe(III) polymerization can also drive the transformation of amorphous (Ca-)Fe(III)-phosphate or -arsenate into ferrihydrite-type precipitates with lower oxyanion uptake capacity, resulting in the concomitant re-solubilization of phosphate or arsenate (McLaughlin and Syers, 1978; Waychunas et al., 1993; Mayer and Jarrell, 2000; Voegelin et al., 2013). The crystallization and transformation of ferrihydrite-type precipitates further reduces their oxyanion sorption capacity (Gerke, 1993; Rea et al., 1994; Majzlan et al., 2007). Ultimately, ferrihydrite-type precipitates can transform into crystalline Fe(III)-(hydr)oxides such as lepidocrocite, goethite, or hematite (Ford, 2002; Cornell and Schwertmann, 2003; Violante et al., 2007), and lepidocrocite can transform into its more stable polymorph goethite (Schwertmann and Taylor, 1972a; Schwertmann and Taylor, 1972b). Co-precipitated oxyanions like silicate, phosphate, or arsenate are not only subject to re-solubilization during precipitate aging, but can also inhibit the polymerization and crystallization

process (Vempati and Loeppert, 1989; Galvez et al., 1999; Ford, 2002) and thereby also affect the release of co-precipitated ions. For example, Fe(III)-precipitates formed in silicate-containing electrolyte have been shown to retain co-precipitated phosphate more effectively than precipitates formed in silicate-free electrolyte (Mayer and Jarrell, 2000).

To date, laboratory studies on the aging of metastable Fe(III)-precipitates mainly addressed the transformation of synthetic ferrihydrite or amorphous Fe(III)-phosphate and Fe(III)-arsenate formed from Fe(III) (McLaughlin and Syers, 1978; Waychunas et al., 1993; Ford, 2002; Cornell and Schwertmann, 2003; Violante et al., 2007; Paktunc et al., 2008; Paktunc et al., 2015). In contrast, the aging of Fe(III)-precipitates formed by the oxidation of dissolved Fe(II) in bicarbonate-buffered solutions at near-neutral pH, i.e., of precipitates formed under conditions representative for many terrestrial and aquatic systems, has received little attention to date. The only study on this topic we are aware of only examined changes in precipitate composition (rather than structure) for a limited set of treatments (Mayer and Jarrell, 2000). Consequently, a comprehensive understanding of the effects of aging on the coupled structural and compositional transformation of Fe(III)-precipitates formed by Fe(II) oxidation in near-neutral waters and their impacts on water chemistry is still lacking to date.

In recent work, we investigated the composition and structure of fresh precipitates formed by Fe(II) oxidation in bicarbonate-buffered solutions at near-neutral pH using an extensive multi-factorial experimental approach to assess the individual and interdependent effects of phosphate, silicate and Ca (Senn et al., 2015). In combination with an earlier time-resolved study (Voegelin et al., 2013), the results revealed how phosphate, silicate and Ca affect precipitate formation, and also showed that – within 4-hours reaction time – precipitate transformation processes already started during Fe(II) oxidation and further structural and compositional precipitate transformation immediately continued after complete Fe(II) oxidation.

This study extends our previous work on fresh Fe(III)-precipitates (Senn et al., 2015) by examining changes in the composition and structure of the same set of Fe(III)-precipitates after aging for 30 d at 40 °C in their synthesis solution. Structural and compositional changes from fresh to aged precipitates and concomitant changes in dissolved phosphate concentrations are interpreted with respect to precipitate type and solution chemistry, with special emphasis on the interdependent effects of phosphate and Ca in the absence or presence of silicate.

2. MATERIALS AND METHODS

2.1. Synthesis of iron precipitates in different background electrolytes

The Fe(III)-precipitation experiments were carried out in analogy to previous work (Roberts et al., 2004; Kaegi et al., 2010; Voegelin et al., 2010; Voegelin et al., 2013; Senn et al., 2015) using the same experimental conditions as described in Senn et al. (2015) (summarized in Table EA1). The aging experiments were performed at an initial pH of 7.0 in six different background electrolytes (Na, Ca, low Ca, Mg, Na+Si and Ca+Si) by the oxidation of 0.5 mM Fe(II) at initial molar phosphate/Fe(II) ratios ($(P/Fe)_{init}$) ranging from 0 to 2. For experiments in Na background electrolyte, 8 mM $NaHCO_3$ were dissolved in high-purity doubly deionized (DDI) water (18.2 M Ω cm, Milli-Q® Element, Millipore) purged with CO_2 gas. Subsequently, the pH was raised to 7.0 (± 0.1) by purging with pressurized air. The Ca background electrolyte was prepared by adding 4 mM $CaCO_3$ to a solution purged with CO_2 gas. After purging, the calcite was dissolved overnight, resulting in a clear solution with a pH of 5-6. The clear solution was purged with pressurized air until the pH was 7.0 (± 0.1). Analogously, to the Ca electrolyte, low Ca background electrolyte was prepared from 0.5 mM $CaCO_3$ and 7 mM $NaHCO_3$, and Mg electrolyte from 4 mM MgO. The silicate-containing electrolytes Na+Si and Ca+Si were prepared by adding 0.5 mM silicate from an alkaline stock solution (100 mM Si from

$\text{Na}_2\text{SiO}_3 \cdot 9\text{H}_2\text{O}$, prepared daily) to the slightly acidic Na and Ca electrolytes after CO_2 purging before raising the pH to 7.0 in order to minimize the formation of silicate polymers (Roberts et al., 2004). According to thermodynamic model calculations, the background electrolytes adjusted to pH 7.0 were in equilibrium with ~ 38 mbar CO_2 and contained ~ 9.5 mM dissolved inorganic carbon. To all electrolytes, $7 \mu\text{M}$ arsenate (0.014 As(V)/Fe) was spiked from a neutral stock solution (13.35 mM As(V) from $\text{Na}_2\text{HAsO}_4 \cdot 7\text{H}_2\text{O}$) after adjusting the pH to 7.0 to study the co-transformation of As(V) during precipitate formation and aging (results to be published separately).

The synthesis of Fe(III)-precipitates was performed with 200 mL of pH-adjusted background electrolyte in 250 mL polypropylene (PP) bottles. Phosphate was spiked using a pH-neutral stock solution ($50 \text{ mM NaH}_2\text{PO}_4 \cdot \text{H}_2\text{O}$). Subsequently, Fe oxidation and precipitation was initiated by adding 0.5 mM Fe(II) from an acidic stock solution ($50 \text{ mM FeSO}_4 \cdot 7\text{H}_2\text{O}$, 1 mM HCl , prepared freshly every day). After agitation to ensure rapid mixing, samples of the unfiltered suspensions were collected and acidified to $0.65\% \text{ HNO}_3$ (Merck, suprapure) for the analysis of total initial concentrations of Fe, P, Si, Na, Ca and Mg. The bottles were closed and left for 4 h, with half-hourly remixing by turning the bottles upside down several times. After this time, Fe was nearly completely ($>99\%$) oxidized. The composition and structure of fresh Fe(III)-precipitates collected after 4 hours reaction time have been discussed in detail in Senn et al. (2015).

The fresh precipitate suspensions in the closed PP bottles were transferred into an oven and aged for 30 d at a constant temperature of 40°C . Once every week, the bottles were turned upside down several times. Before sampling, the settled precipitates were again re-suspended by gentle shaking. The final pH after 30 d reaction time was measured in unfiltered suspension aliquots. Samples for determination of Fe, P, Si, Na, Ca and Mg concentrations in unfiltered

suspensions and filtered solutions (0.1 μm cellulose nitrate) were collected and acidified to 0.65% HNO_3 (Merck, suprapure). This acidification was sufficient to achieve complete dissolution of precipitates in the unfiltered suspensions within a few hours. For transmission electron microscopy (TEM), precipitates were collected on TEM grids (Lacey-carbon Cu, Okenshoji Co. LTD, Japan) by depositing 20 μL of suspension on the grid and using a paper tissue to draw the solution through the grid. The grids were immediately immersed in DDI water to remove soluble salts and subsequently dried in a desiccator. Precipitate samples for analysis by X-ray absorption spectroscopy (XAS) were collected by filtration of the remaining suspension volume through cellulose nitrate filters (0.1 μm). The filters were washed by passing 20 mL of DDI water and dried under a stream of dry air. Precipitate powders and TEM grids were stored in a desiccator until analysis. In this manuscript, labels for individual treatments are composed of the respective background electrolyte and the $(\text{P}/\text{Fe})_{\text{init}}$ (e.g., Na 0.05 for experiments performed in Na electrolyte at $(\text{P}/\text{Fe})_{\text{init}}$ of 0.05).

To assess the effect of 0.014 As(V)/Fe in the multifactorial experiment on the structure of fresh and aged Fe(III)-precipitates formed in the phosphate- and silicate-free Na, Mg, low Ca and Ca electrolytes, these precipitates were also synthesized in the absence of arsenate.

2.2. ICP-MS analyses

Acidified unfiltered and filtered samples were diluted with aqueous 0.65% HNO_3 solution as required for the analysis of Fe, P, Si, Na, Ca and Mg by inductively coupled plasma mass spectrometry (ICP-MS; Agilent 7500ce). The amounts of P and Fe in the precipitates (P_{ppt} , Fe_{ppt}) were calculated from their total concentration in the initial solution and their dissolved concentration in the final filtered suspension. In general, the P concentrations measured in filtered samples (P_{filt}) were assumed to correspond to dissolved concentrations (P_{soln}). As for the fresh precipitate suspensions (Senn et al., 2015), however, elevated Fe concentrations in some of

the filtered aged Na and Na+Si suspensions (Fe_{filt}) pointed to the presence of colloidal Fe that was not completely retained on the filter membranes. Therefore, the dissolved P concentrations in the aged Na and Na+Si electrolyte suspensions were calculated from the concentrations of Fe and P in the filtered suspensions assuming that Fe_{filt} corresponded to colloidal Fe with a P/Fe ratio equal to the P/Fe ratio of the Fe(III)-precipitate retained on the filter membrane. In general, this correction was small (<10% of P_{filt} in colloidal form), except for the treatments Na+Si 0.50 and Na+Si 0.94, with 27% and 29% of P_{filt} in colloidal form.

2.3. X-ray absorption spectroscopy

For Fe K-edge extended X-ray absorption fine structure (EXAFS) spectroscopy in transmission mode, the dried precipitate samples (~10 mg) were mixed with cellulose (~140 mg) and pressed into 13-mm diameter pellets as described in Senn et al. (2015). The samples were measured at the XAS beamline at the Angströmquelle Karlsruhe (ANKA, Eggenstein-Leopoldshafen, Germany) and at the Swiss Norwegian Beamline (SNBL) at the European Synchrotron Radiation Facility (ESRF, Grenoble, France) at room temperature with the same settings as described in Senn et al. (2015). For the extraction of the sample spectra and for their analysis by linear combination fitting (LCF; k -range 2-11 \AA^{-1}), the software code Athena was used (Ravel and Newville, 2005). For principal component analysis (PCA) of sets of sample spectra and target testing (TT) of reference spectra (Isaure et al., 2002; Manceau et al., 2002), software from beamline 10.3.2 at the Advanced Light Source (ALS, Berkely, USA) was used (Marcus et al., 2004). For LCF analysis, reference spectra of representative structural/spectral endmembers were derived from the spectra of selected precipitates as described in detail in section 3.2.1. In addition, the spectra of two synthetic ferrihydrite-type precipitates, Fh and HFO, were used for LCF analysis that have been described previously (Voegelin et al., 2010; Voegelin et al., 2013; Senn et al., 2015). The Fh reference corresponds to 2-line ferrihydrite synthesized

according to a standard protocol, the HFO reference represents a silicate-containing ferrihydrite-type precipitate (Si/Fe ~0.56) that was synthesized by forced Fe(III) hydrolysis in the presence of silicate. Compared to Fh, the HFO exhibits a similar degree of edge-sharing linkage of Fe(III)-octahedra, but reduced corner-sharing linkage. For the analysis of spectra from a specific electrolyte by LCF, the two (Na+Si and Ca+Si electrolytes) or three (Na, low Ca, Mg and Ca electrolytes) relevant reference spectra were considered. Starting with the best one-component fit, the number of components n was increased as long as the normalized sum of squared residuals ($\text{NSSR} = \frac{\sum (\text{data}_i - \text{fit}_i)^2}{\sum \text{data}_i^2}$) of the best $n+1$ -component fit was at least 10% (relative) lower than the NSSR of the best n -component fit. Individual fractions were constrained to positive values but the sum of all fractions was not constrained. For data interpretation, however, the LCF-derived fractions were normalized to a sum of unity.

2.4. Electron microscopy

Scanning transmission electron microscope (STEM) analyses were performed on a STEM (HD2700Cs, Hitachi, Japan) operated at 200 kV. Electron microscopy (EM) images were collected using a secondary electron (SE) detector and a high-angle annular dark field (HAADF) detector. Elemental analysis, including elemental distribution maps, were acquired with DigitalMicrograph (V.1.82, Gatan Inc., CA, USA) using an EDX detector (EDAX, NJ, USA). Signal processing was done using DigitalMicrograph.

2.5. Thermodynamic calculations

Thermodynamic calculations of saturation indices were performed with PHREEEQC using the MinteqA2 V4 database (Parkhurst and Appelo, 1999), complemented with an alternative solubility product of octacalciumphosphate from Tung et al. (1988) ($\text{pK}_{\text{so}} = 48.4 \pm 0.1$ at 23.5 °C).

3. RESULTS

3.1. pH and total Ca, P and Fe concentrations of aged suspensions

After the formation of the fresh precipitates (4 h reaction time), the pH of the suspensions corresponded to initial values of pH 7.0 ± 0.1 , and total element concentrations deviated less than 5% from their initial values (Senn et al., 2015). During the 30 days aging period, the pH of the suspensions increased to pH 7.9 ± 0.3 ($n=104$) (Fig. EA1), probably due to the outgassing of CO_2 . In the Ca and Ca+Si electrolytes at the lowest $(\text{P/Fe})_{\text{init}}$, the increase in pH was least pronounced, due to the counteracting effect of Ca-carbonate precipitation, which can only proceed at low phosphate concentrations (Plant and House, 2002). This interpretation was supported by the recovery data for Ca (total Ca concentration in unfiltered suspension after aging divided by total Ca concentration in unfiltered initial solution), which showed that up to 45% of the Ca was lost from suspension at the lowest $(\text{P/Fe})_{\text{init}}$ (Fig. EA2). Together with Ca, up to 20% of the total phosphate at the lowest $(\text{P/Fe})_{\text{init}}$ was lost from the suspension (Fig. EA2), most probably due to co-precipitation with Ca-carbonate (Plant and House, 2002) on the walls of the PP bottles. At the highest $(\text{P/Fe})_{\text{init}}$, on the other hand, the loss of up to 10% of the Ca and up to 28% of the phosphate from the aged Ca and Ca+Si suspensions (Fig. EA2) was probably due to the formation of Ca-phosphate on the walls of the bottles. The postulated formation of Ca-carbonate at the lowest $(\text{P/Fe})_{\text{init}}$ and of Ca-phosphate at the highest $(\text{P/Fe})_{\text{init}}$ was supported by the XRD patterns of the precipitates Ca 0 A and Ca 1.55 A, which revealed minor peaks of calcite and apatite (HAP), respectively (Fig. EA10). For the precipitate formed in phosphate-free Ca+Si electrolyte, on the other hand, Ca K-edge XANES spectroscopy pointed to the formation of aragonite rather than calcite (not shown), probably due to the stabilizing effect of silicate on aragonite that slows down its transformation into calcite (Kellermeier et al., 2013).

In the silicate-containing electrolytes, Fe remained nearly completely recoverable after aging (recovery >96% for 90% of the samples; Fig. EA2). The negligible loss of Fe(III)-

precipitates most probably reflected their colloidal stabilization by sorbed silicate (Mayer and Jarrell, 1996) as well as by phosphate at high $(P/Fe)_{init}$, noting that high phosphate levels also stabilized Fe(III)-precipitates in the silicate-free electrolytes. Only at low $(P/Fe)_{init}$ in silicate-free electrolytes, losses of up to ~10% of the total Fe were observed (35% in low Ca electrolyte at $(P/Fe)_{init}$ of 0). Since poorly-crystalline lepidocrocite was the dominant precipitate in these latter treatments, the Fe losses are attributed to the attachment of weakly-charged lepidocrocite (point of zero charge ~6.7-7.5; (Cornell and Schwertmann, 2003)) to the walls of the PP bottles. In general, however, the recovery data showed that the solids isolated from the aged suspensions by filtration for analysis by XAS, TEM and XRD were representative for the aged Fe(III)-precipitates.

The results from additional aging experiments conducted under the same or comparable conditions indicated that, in general, the experiments were reproducible with respect to dissolved phosphate concentration after aging (Fig. EA3). The reproducibility of the observed effects was also indicated by the consistent trends in solid phase speciation and dissolved phosphate concentrations as a function of $(P/Fe)_{init}$ in individual electrolytes as well as between electrolytes (see sections 3.2 and 3.3).

3.2. Fe(III)-precipitate characterization by Fe K-edge EXAFS spectroscopy

All aged precipitates were characterized with Fe K-edge EXAFS spectroscopy (Fig. EA8). In Fig. 1, the spectra of selected precipitates aged in the Na and Ca+Si electrolytes are compared to spectra of the respective fresh precipitates. Visual comparison and difference spectra reveal that significant structural changes occurred during the aging of precipitates formed in the Na electrolyte up to a $(P/Fe)_{init}$ of ~0.75. In contrast, the spectra of samples formed in the Ca+Si electrolyte suggested that no detectable changes in Fe coordination occurred during aging. To

gain more quantitative insight into the structure of the aged precipitates and into structural changes during aging, the spectra of all aged precipitates were analyzed by LCF.

3.2.1. Reference spectra for LCF analysis of Fe K-edge EXAFS spectra

Evaluation of the Fe K-edge EXAFS spectra of the 72 aged precipitates by principal component analysis (PCA) suggested that the first four PCA-components represented the dominant spectral features (Fig. EA4a), as previously found for the 72 spectra of fresh precipitates (Senn et al., 2015). Target testing showed that the first four PCA-components derived from the spectra of the fresh precipitates could be adequately reproduced by the first four PCA-components derived from the spectra of the aged precipitates (Fig. EA4b). This suggested that the spectra of the aged precipitates could be described with similar spectral components as the fresh precipitates.

For the fresh precipitates, we derived four spectra from the 72 sample spectra that represented distinct structural endmembers. We then combined these “endmember spectra” with one independent reference spectrum to analyze all sample spectra by LCF (Senn et al., 2015). Briefly, the four endmember spectra and the independent reference spectrum can be described as follows: (1) FeP*: amorphous Fe(III)-phosphate; average of the spectra of precipitates formed at the highest $(P/Fe)_{\text{init}}$ (1.5 and 2) in the Na and Na+Si electrolytes; also representing Fe(III)-phosphate formed in Mg electrolyte. (2) CaFeP*: amorphous Ca-Fe(III)-phosphate (containing structural Ca and with higher P/Fe ratio and higher degree of Fe-Fe linkage than FeP*); average of the spectra of precipitates formed at the highest $(P/Fe)_{\text{init}}$ (1.5 and 2) in the Ca and Ca+Si electrolytes. (3) Fh-Si*: silicate-containing ferrihydrite; average of the spectra of the precipitates formed in the Na+Si and Ca+Si electrolytes in the absence of phosphate. (4) pcLp*: poorly crystalline lepidocrocite; average of the spectra of the precipitates formed in the silicate-free Na, Ca, low Ca and Mg electrolytes in the absence of phosphate. (5) HFO: reference spectrum of

ferrihydrite-type hydrous ferric oxide with lower degree of corner-sharing Fe-Fe linkage than in 2-line ferrihydrite; used to represent the transformation product of (Ca-)Fe(III)-phosphate in the silicate-free electrolytes. In addition, the spectrum lowCaFeP* (amorphous Ca-Fe(III)-phosphate formed at $(P/Fe)_{init}$ of 1.5 and 2 in the low Ca electrolyte) was used in the LCF analysis of spectra from the low Ca electrolyte. However, this spectrum did not represent an independent spectral component as it could be described as a linear combination of the spectra FeP* and CaFeP* (Senn et al., 2015). Although visual examination of the PCA-components provided only evidence for four major spectral components in the dataset, five different spectra (without lowCaFeP*) were used to describe the experimental spectra. This apparent discrepancy can be attributed to the relatively small differences between the spectra FeP* and CaFeP* and between the spectra Fh-Si* and HFO (Fig. 2) and to the fact that the different references consist of similar basic structural units. The four spectral components derived from PCA may thus rather represent the main structural variations that define the different precipitate fractions (extent of distortion in FeO_6 -octahedra and of second-shell Fe coordination with edge- and corner-sharing Fe and with P) than the individual precipitate types.

The analogous set of endmember spectra as previously derived from the spectra of fresh precipitates (Senn et al., 2015) were derived from the spectra of the aged precipitates (Fig. EA5). In Fig. 2, the endmember spectra derived from aged samples (FeP*a, CaFeP*a, lowCaFeP*a, Fh-Si*a, and pcLp*a) are compared to the endmember spectra derived from fresh precipitates (FeP*, CaFeP*, lowCaFeP*, Fh-Si*, and pcLp*).

The spectra of fresh and aged FeP, CaFeP, lowCaFeP, and Fh-Si are nearly identical, showing that the aging of these structural endmembers did not induce marked changes in local Fe coordination. In contrast, the spectrum of aged poorly-crystalline lepidocrocite (pcLp*a) derived from the precipitates aged in the silicate-free background electrolytes in the absence of

phosphate exhibited a higher second-shell amplitude than the spectrum of freshly precipitated poorly crystalline Lp (pcLp*) (Fig. 2), pointing to an increase in the order of local Fe coordination during aging. Comparison of the Fourier-transformed EXAFS spectrum pcLp*a with the spectrum of crystalline Lp showed that the amplitude of the second-shell of the spectrum pcLp*a was nearly as high, but that the amplitudes of peaks at higher distances were still significantly reduced (Fig. EA6), indicating that local Fe coordination in the aged poorly crystalline Lp was still less ordered than in crystalline Lp. Analysis of the XRD patterns of the fresh and aged precipitates Na 0 and Ca 0 using the Scherrer equation indicates an increase of the coherently scattering domain size from $\sim 2.3 \pm 0.1$ nm (Senn et al., 2015) to $\sim 2.9 \pm 0.1$ nm (Fig. EA10) perpendicular to the lepidocrocite sheets during aging. On the other hand, the results show that also after aging, the poorly crystalline lepidocrocite still consisted of only few stacked sheets.

For fresh precipitates formed in the silicate-containing Na+Si and Ca+Si electrolytes, we previously showed that the two respective endmember spectra (Fh-Si* and FeP* for Na+Si electrolyte; Fh-Si* and CaFeP* for Ca+Si electrolyte) were sufficient to describe all sample spectra (Senn et al., 2015). The same was also true for the respective aged precipitates. In contrast, for fresh precipitates formed in the silicate-free Na, low Ca, Mg and Ca electrolytes, we previously found that a third reference spectrum in addition to the two endmembers of each background electrolyte (pcLp* and FeP*, CaFeP* or lowCaFeP*) was required to reproduce the sample spectra (Senn et al., 2015). This additional spectral component was best described by the reference HFO, a silicate-containing ferrihydrite-type precipitate that represented the phosphate-rich ferrihydrite-type precipitate formed by fast transformation of initially precipitated (Ca-)Fe(III)-phosphate (Voegelin et al., 2013; Senn et al., 2015). Analogously, PCA of the spectra of aged precipitates from the silicate-free Na electrolyte showed that, in addition to the two

endmember spectra pcLp*a and FeP*, a third reference spectrum was required to reproduce all sample spectra. LCF analysis of the 9 samples from the Na electrolyte formed at $(P/Fe)_{init}$ from 0.05 to 1.0 using either the spectrum of 2-line ferrihydrite (Fh), hydrous ferric oxide (HFO) or a numerical 50/50 mixture of these two spectra (Fh/HFO) as third reference spectrum showed that the use of Fh/HFO and the Fh spectrum lead to markedly better fits than the HFO spectrum (Table EA2). Among the reference spectra Fh and Fh/HFO, the Fh spectrum returned slightly better fits for the 3 samples with the highest ferrihydrite-type fraction, the Fh/HFO spectrum for the 6 samples with lower ferrihydrite-type fractions (Table EA2). Whether Fh/HFO or Fh was used as ferrihydrite-type reference spectrum did not markedly affect the fit results for pcLp*a, but the use of the Fh/HFO spectrum for LCF resulted in higher ferrihydrite-type precipitate fractions and lower FeP* fractions than the use of the Fh spectrum (Table EA2, Fig. EA7). As we used the Fh/HFO spectrum for further data evaluation by LCF, it should thus be kept in mind that the respective LCF results represent an upper estimate for the degree of Fe(III)- or Ca-Fe(III)-phosphate transformation into a ferrihydrite-type phase during aging.

Based on the above considerations, the following six spectra were used for the interpretation of the Fe K-edge EXAFS spectra of aged precipitates by LCF: FeP*, CaFeP*, lowCaFeP*, Fh-Si*, pcLp*a and Fh/HFO. For each background electrolyte, only the two (electrolytes with Si) or three (electrolytes without Si) relevant reference spectra were used for LCF analysis, as summarized in Table EA3.

3.2.2. LCF analysis of Fe K-edge EXAFS spectra

In Fig. 3, the normalized LCF fractions for the aged precipitates are shown together with the LCF results for fresh precipitates from Senn et al. (2015). The complete LCF results for the aged samples are listed in Table EA4. As for the fresh precipitates, the results reveal a shift from lepidocrocite (without silicate) or ferrihydrite (with silicate) in the phosphate-free treatments to

Fe(III)-phosphate (without Ca) or Ca-Fe(III)-phosphate (with Ca) at the highest $(P/Fe)_{init}$ of ~ 1.5 and ~ 2 (Fig. 3). To visualize structural changes induced by aging, the difference between the LCF results for aged and fresh precipitates are displayed in the panels on the right of Fig. 3. The difference graphs demonstrate that the largest structural changes occurred in the Na electrolyte at intermediate $(P/Fe)_{init}$ and that no substantial changes occurred in the Ca+Si and Ca electrolyte, in line with the comparison of the spectra of selected fresh and aged precipitates from the Na and Ca+Si electrolytes in Fig. 1. The results for the Mg, low Ca and Na+Si electrolytes further demonstrated that silicate as well as Ca or (to a lesser degree) Mg in suspension reduced the extent of precipitate transformation during aging.

3.2.3. EXAFS analysis of fresh and aged precipitates formed in arsenate-free electrolytes

In the absence of interfering oxyanions other than bicarbonate, Fe(II) oxidation in bicarbonate-buffered solutions at neutral pH has previously been shown to lead to the formation of poorly crystalline lepidocrocite and a minor fraction of goethite (Schwertmann et al., 1984; Voegelin et al., 2010; Voegelin et al., 2013). Dissolved phosphate at P/Fe ratios as low as 0.02-0.03 on the other hand completely inhibits goethite formation in bicarbonate-buffered neutral solutions (Cumplido et al., 2000; Voegelin et al., 2010). For fresh Fe(III)-precipitates from the multifactorial experiment, Fe K-edge XAS and XRD results showed that no goethite was present in precipitates formed in the phosphate- and silicate-free background electrolytes (Senn et al., 2015). Based on the assumption that arsenate exhibits a similar influence on Fe(III) polymerization as phosphate, the absence of goethite was attributed to the 0.014 As(V)/Fe (7 μ M As(V)) present in all suspensions from the multifactorial experiment (added to study As(V) removal; results to be published separately).

To assess the effect of 0.014 As(V)/Fe on precipitate structure and transformation in the multifactorial experiment, additional Fe(III)-precipitates formed in phosphate- and silicate-free

Na, Ca, low Ca and Mg electrolytes without As(V) addition were analyzed by Fe K-edge EXAFS spectroscopy (Fig. EA9). For the fresh As-free precipitates, LCF with the pcLp* endmember and a goethite reference spectrum indicated the formation of a small fraction of goethite in the Na, low Ca and Mg electrolytes (Fig. 4, Fig. EA9a; Table EA6), confirming that the absence of a minor goethite fraction in the fresh Na 0, low Ca 0, Mg 0 and Ca 0 samples from the multifactorial experiment was due to the presence of 0.014 As(V)/Fe in the suspensions and that arsenate affected Fe(III) polymerization like similarly low levels of phosphate.

For the aged As-free precipitate formed in phosphate- and silicate-free Na electrolyte, LCF analysis revealed that it consisted of ~78% goethite and only 22% poorly crystalline Lp (represented by pcLp*a endmember spectrum). Thus, about 75% of the initially formed pcLp* had transformed into goethite during precipitate aging (Fig. 4, Fig. EA9b, Table EA6). In contrast, no goethite was detected by XRD in the aged precipitate Na 0 formed in the presence of 0.014 As(V)/Fe (Fig. EA10), showing that this As(V) level was sufficient to inhibit goethite formation during aging.

Because low levels of arsenate were found to have a similar effect on Fe(III) polymerization as phosphate and even the lowest studied $(P/Fe)_{init}$ ratio of 0.05 in the multifactorial experiment was more than 3 times higher than the As(V)/Fe ratio of 0.014 and at least 1.6 times higher than the P/Fe ratio required to inhibit goethite formation (Cumplido et al., 2000; Voegelin et al., 2013), and because silicate at a $(Si/Fe)_{init}$ of 1.0 inhibited the formation of crystalline Fe(III)-(hydr)oxide in the phosphate-free Na+Si and Ca+Si electrolytes, we concluded that the effect of 0.014 As(V)/Fe on precipitate structure was negligible in all treatments of the multifactorial experiment except the four precipitates Na 0, low Ca 0, Mg 0 and Ca 0 formed in the absence of phosphate and silicate.

Remarkably, LCF analysis of the aged As-free precipitates formed in phosphate- and silicate-free suspensions showed that the goethite fraction drastically decreased from the Na (~78%) over the low Ca (~58%) and Mg (~23%) to the Ca electrolyte (~5%), suggesting that also Ca and Mg in addition to phosphate and arsenate may interfere with the transformation from lepidocrocite to goethite (Fig. 4, Fig. EA9, Table EA6). However, further experiments on this effect were beyond the scope of this study.

3.3. EM analysis of Fe(III)-precipitates

Secondary electron (SE) images of fresh and aged precipitates formed at $(P/Fe)_{init}$ of 0, ~0.5 and ~2 in Na electrolyte are shown in Fig. 5a-f, additional high-angle annular dark field (HAADF) and SE images for the aged precipitate formed at $(P/Fe)_{init}$ of ~0.5 in Fig. 5g-i. The morphologies of the fresh precipitates indicated the formation of aggregates of lepidocrocite platelets at a $(P/Fe)_{init}$ of 0 and of aggregates of spherical Fe(III)-phosphate particles with smooth particle surfaces at a high $(P/Fe)_{init}$ of ~2, as observed in previous work (Kaegi et al., 2010; Voegelin et al., 2013). Aging appeared to induce a slight coarsening of the lepidocrocite platelets in the phosphate-free Na electrolyte (Fig. 5d versus Fig. 5a), qualitatively in line with the small increase in sheet stacking observed by XRD (see section 3.2.1). For amorphous Fe(III)-phosphate formed at $(P/Fe)_{init}$ ~2, the EM images did not reveal any apparent morphological changes during aging (Fig. 5f versus Fig. 5c).

Marked morphological changes were observed for the precipitate formed at $(P/Fe)_{init}$ of ~0.5. Whereas the fresh precipitate exhibited the morphology of amorphous Fe(III)-phosphate (Fig. 5b), the aged precipitate consisted of a mixture of thin lepidocrocite platelets and spherical particles with rough surfaces, as revealed by the corresponding SE and HAADF images (Fig. 5e and Fig. 5h). In previous work, we observed that ferrihydrite crystallites formed by Fe(II) oxidation in water aggregate into spherical nanoparticles with a rougher surface than spherical

Fe(III)-phosphate nanoparticles (Kaegi et al., 2010). The morphological changes observed for the precipitate formed at $(P/Fe)_{init}$ of ~ 0.5 in the Na electrolyte are thus in agreement with the XAS results, which indicated that the precipitate transformed from an amorphous Fe(III)-phosphate to 83% Fh/HFO and 17% pcLp*_a during aging (Fig. 3). Additional SE images with higher resolution (Fig. 5g,i) suggested that the lepidocrocite platelets in the aged precipitate were covered with Fh/HFO particles. The XRD pattern of an aged precipitate formed at $(P/Fe)_{init}$ of 0.52 did not show any lepidocrocite peaks (Fig. EA10), suggesting that the Lp platelets (which accounted for only a small fraction of the total precipitate based on XAS; Fig. 3) were highly disordered.

EM images of aged and fresh precipitates formed at $(P/Fe)_{init}$ of 0, ~ 0.5 and ~ 2 in Ca electrolyte (Fig. EA12) revealed precipitate morphologies in line with XAS (Fig. 3) and XRD (Fig. EA10) results and provided no evidence for changes in morphology during aging.

3.4. Dissolved phosphate in suspension

In Fig. 6 the absolute and relative dissolved concentrations of phosphate in the aged suspensions are shown as a function of $(P/Fe)_{init}$ in comparison to the concentrations in the fresh suspensions. For fresh precipitate suspensions, we have shown in our previous work (Senn et al., 2015) that trends in dissolved phosphate as a function of $(P/Fe)_{init}$ change around a critical $(P/Fe)_{init}$ (referred to as $(P/Fe)_{crit}$). For a specific electrolyte, this $(P/Fe)_{crit}$ represents the minimal $(P/Fe)_{init}$ required for exclusive formation of amorphous Fe(III)- or Ca-Fe(III)-phosphate. At $(P/Fe)_{init} < (P/Fe)_{crit}$, low dissolved phosphate concentrations reflected effective removal of phosphate by the fresh precipitates. At $(P/Fe)_{init} > (P/Fe)_{crit}$, markedly increasing dissolved phosphate concentrations with increasing $(P/Fe)_{init}$ reflected that additional phosphate could not be co-precipitated with Fe.

In the aged Na, Mg, low Ca, and Na+Si suspensions, the concentrations of phosphate at $(P/Fe)_{init} \cdot 1$ (i.e., $> (P/Fe)_{crit}$ in all electrolytes) closely matched the concentrations in the fresh suspensions, suggesting that neither further phosphate precipitation nor phosphate re-solubilization occurred to a substantial extent during aging. In the Ca and Ca+Si electrolytes, in contrast, dissolved phosphate concentrations in suspensions with $(P/Fe)_{init} \cdot 1$ substantially decreased during aging. Taking also the trends in total Ca and phosphate in suspension at high $(P/Fe)_{init}$ and the XRD pattern of the sample Ca 1.55 A into account (section 3.1), the decrease in dissolved phosphate was attributed to the precipitation of Ca-phosphate (which mainly attached to the walls of the reaction vessels). Thermodynamic calculations based on the dissolved concentrations of phosphate and Ca and on solution pH in the aged Ca electrolyte with $(P/Fe)_{init}$ of 1.5 (section EA7) indicated that the solution was undersaturated with respect to brushite, but around saturation with respect to octacalciumphosphate (OCP), which is a precursor in the precipitation of hydroxyapatite (Feenstra and De Bruyn, 1979). In the aged low Ca electrolyte suspensions, saturation with respect to OCP was only reached at $(P/Fe)_{init}$ of ~ 2 , suggesting that Ca-phosphate precipitation was negligible over most of the studied range in $(P/Fe)_{init}$.

At a $(P/Fe)_{init} < \sim 0.75-1.0$ in the Na, Mg, low Ca, and Ca electrolytes, an increase in the dissolved phosphate fractions of the aged suspensions was observed with decreasing $(P/Fe)_{init}$, whose intensity followed the order $Na \gg Mg \sim low\ Ca \gg Ca$. The increase in dissolved phosphate fractions corresponded to apparent plateaus in absolute phosphate concentrations at ~ 0.18 mM in the Na electrolyte, $\sim 0.05-0.07$ mM in the low Ca and Mg electrolytes, and ~ 0.03 mM in the Ca electrolyte, before the concentrations decreased towards 0 in the phosphate-free treatments (Fig. 6). Comparison with the respective relative and absolute concentrations of phosphate in the fresh suspensions clearly revealed substantial phosphate release into solution during aging whose extent depended on the valence and concentration of the electrolyte cation.

In the Na+Si electrolyte, a plateau in dissolved phosphate at a similar concentration as in the Mg and low Ca electrolytes was observed in the $(P/Fe)_{init}$ range from ~0.2-0.6, indicating that silicate also reduced phosphate release during aging. The lowest dissolved relative phosphate concentrations at $(P/Fe)_{init}$ of 0.1-0.6 were observed in aged Ca+Si electrolyte suspensions, due to the combined effects of Ca and silicate on precipitate aging and phosphate release.

In Fig. 7, the concentrations of dissolved phosphate in fresh and aged precipitate suspensions at $(P/Fe)_{init}$ of 0.05, 0.1, 0.2 and 0.5 in different background electrolytes are compared. The plots reflect the previously described trends in phosphate co-precipitation and re-solubilization. They further emphasize that – also at the lowest $(P/Fe)_{init}$ of 0.05 – most effective phosphate retention in fresh and aged precipitate suspensions was achieved in the Ca+Si electrolyte.

Based on the concentrations of dissolved phosphate in the aged suspensions and the initial total concentrations of Fe and phosphate, the molar ratio of precipitated phosphate over Fe $(P/Fe)_{ppt}$ was calculated for all treatments (Table EA4). For suspensions with $(P/Fe)_{init}$ of ~0.2-0.75, i.e. between the phosphate uptake capacity of fresh ferrihydrite-type and (Ca-)Fe-phosphate-type precipitates, respectively, the $(P/Fe)_{ppt}$ and the LCF-derived fractions were used to derive the solid-phase P/Fe ratios of the individual structural units in the Na, Mg, low Ca and Na+Si electrolytes by multiple linear regression (details in section EA6). Analogous calculations for the Ca and Ca+Si electrolytes were not performed because phosphate partly also precipitated as Ca-phosphate or phosphate-containing Ca-carbonate during aging. The results for the Na, Mg and low Ca electrolytes indicated that the ferrihydrite-type transformation product of Fe(III)-phosphate in the aged suspensions had a P/Fe ratio of ~0.10-0.16. For the Na+Si electrolyte, the calculation returned a P/Fe ratio of 0.09 for the ferrihydrite fraction (Table EA7).

4. DISCUSSION

4.1. Precipitate transformation and phosphate release during aging

The comparison of the results on Fe precipitate structure and dissolved phosphate in fresh and aged suspensions (Fig. 1, Fig. 3 and Fig. 6) reveals that substantial precipitate transformation occurred during the aging of the suspensions that also affected phosphate sequestration. The most prominent change in Fe(III)-precipitate structure during aging was the transformation of Fe(III)-phosphate and to a much lesser extent Ca-Fe(III)-phosphate into a ferrihydrite-type Fe(III)-precipitate with lower (P/Fe) ratio, i.e., lower phosphate retention capacity. This process was most pronounced at intermediate $(P/Fe)_{\text{init}}$ ratios ~ 0.3 - 0.5 (Fig. 3) and resulted in the release of initially precipitated phosphate (Fig. 6). The extent of (Ca-)Fe(III)-phosphate transformation and phosphate release depended on the background electrolyte cation and on the absence/presence of silicate (Fig. 3 and Fig. 6). Further changes in Fe(III)-precipitate structure during aging included the polymerization of the ferrihydrite-like transformation product of Fe(III)-phosphate (from HFO to Fh/HFO) (Fig. 2) and the crystallization of lepidocrocite in the silicate-free background electrolytes (Fig. 2 and Fig. EA6). The different transformation processes and their dependence on precipitate composition and solution chemistry are discussed in the following sections.

4.2. Stability and transformation of Fe-phosphate and Ca-Fe(III)-phosphate during aging

4.2.1. Structure of fresh (Ca-)Fe(III)-phosphate precipitates (Senn et al., 2015)

For freshly precipitated (Ca-)Fe(III)-phosphate, we previously found that the structure and composition depended on the background electrolyte cation and could be described based on (mixtures of) different polymeric units (Senn et al., 2015). Compared to Fe(III)-phosphate formed in Na electrolyte, Mg did not detectably affect the local Fe coordination in Fe(III)-

phosphate, but electrostatically enhanced co-precipitation of phosphate with bivalent Mg led to more effective phosphate uptake than co-precipitation with monovalent Na. A low Ca concentration of 0.5 mM had a similar effect as 4 mM Mg, and was also mainly attributed to electrostatic interactions. At a Ca concentration of 4 mM in the Ca and Ca+Si electrolytes, amorphous Ca-Fe(III)-phosphate formed whose structure and composition could be rationalized by a mixture of (i) amorphous Fe(III)-phosphate polymers analogous to the ones formed in the Mg and Na electrolytes, (ii) mitridatite-like Ca-Fe(III)-phosphate polymers with enhanced Fe-Fe linkage and higher P/Fe ratio, and (iii) Ca-phosphate polymers.

4.2.2. Aging of Fe(III)-phosphate and Ca-Fe(III)-phosphate in silicate-free electrolytes

In the Na electrolyte, partial Fe(III)-phosphate transformation into a ferrihydrite-type phase (Fh/HFO) during aging was observed at $(P/Fe)_{init} \bullet 0.75$, and complete transformation at $(P/Fe)_{init} \bullet 0.4$ (Fig. 1 and Fig. 3; Fig. 8). The concomitant increase in dissolved phosphate up to a plateau concentration of ~ 0.18 mM (Fig. 6) suggests that this phosphate concentration corresponded to the minimum concentration required to inhibit (further) Fe(III)-phosphate transformation in the absence of other interfering ions.

Although Mg does not markedly affect local Fe coordination in fresh Fe(III)-phosphate compared to Fe(III)-phosphate formed in Na electrolyte (Senn et al., 2015), the extents of structural Fe(III)-phosphate transformation (Fig. 3) and of dissolved phosphate release (Fig. 6) during precipitate aging in the Mg electrolyte were markedly reduced relative to the Na electrolyte. This difference suggests that electrostatic interactions between Mg and phosphate stabilized the Fe(III)-phosphate and reduced the driving force for further Fe polymerization. The phosphate plateau concentration of ~ 0.065 mM from $(P/Fe)_{init}$ of ~ 0.75 down to ~ 0.2 , i.e., for precipitates with Fe(III)-phosphate fractions from 74% to 9% (Fig 3, Table EA4), suggests that (further) Fe(III)-phosphate transformation was effectively inhibited. The lower plateau

concentration of phosphate than in the Na electrolyte further points to a higher stability of Fe(III)-phosphate in the Mg than in the Na electrolytes.

Nearly identical results as in the Mg electrolyte were also observed in the low Ca electrolyte (Fig. 3, Fig. 6), indicating that 0.5 mM Ca mainly affected precipitate stability via electrostatic interactions similar to Mg rather than more specific interactions between Ca and phosphate, in line with the result that saturation with respect to OCP in the aged low Ca suspensions was only reached at $(P/Fe)_{init}$ of 1.5 or even higher (Table EA8).

In the Ca electrolyte, Ca-phosphate precipitation led to a pronounced decrease in dissolved phosphate during aging of suspensions with $(P/Fe)_{init} \cdot 1$ (Fig. 6) and also seemed to limit phosphate resolubilization in suspensions with $(P/Fe)_{init}$ from 0.1 to 0.75 (compared to Na, Mg and low Ca electrolytes), as reflected by an average phosphate concentration of $22 \pm 6 \mu\text{M}$ for $(P/Fe)_{init}$ from 0.1 to 1.5 ($n=9$) that was in line with solubility control by OCP (phosphate concentration of $26 \mu\text{M}$ or $9 \mu\text{M}$ using OCP solubility products from MinteqA2 V4 database or Tung et al. (1988), respectively; calculated for an average Ca concentration of $3.5 \pm 0.2 \text{ mM}$ and an average pH of 7.9 ± 0.1 in the respective suspensions). Despite this effective phosphate sequestration process, the extent of Ca-Fe(III)-phosphate transformation in the Ca electrolyte was markedly reduced compared to the Na, Mg and low Ca electrolytes (Fig. 3, Fig. 8). The pronounced recalcitrance of Ca-Fe(III)-phosphate in the Ca electrolyte towards transformation during aging may be attributed to three factors: (i) Favorable electrostatic interactions between precipitated Ca and phosphate that stabilize the precipitate, in analogy to Fe(III)-phosphate formed in Mg electrolyte. (ii) Presence of mitridatite-like Ca-Fe(III)-polymers with Fe-Ca polyhedral linkage and higher degree of Fe-Fe linkage than other Fe(III)-phosphate polymers that hampers further Fe(III) polymerization during aging. (iii) Presence of intermixed Ca-phosphate polymers that may inhibit Fe(III) polymerization (and whose fraction increases with

increasing $(P/Fe)_{init}$ (Senn et al., 2015)). The effective stabilization of Ca-Fe(III)-phosphate by Ca observed in the 30-days aging experiment is in line with the observation of recalcitrant amorphous Ca-Fe(III)-phosphate in environmental systems, for example in Fe accumulations with ages between decades and millennia in sediments from Lake Baikal (Deike et al., 1997; Och et al., 2012).

4.2.3. Aging of Fe(III)-phosphate and Ca-Fe(III)-phosphate in silicate-containing electrolytes

Precipitate aging in the Na+Si electrolyte resulted in a markedly lower phosphate release than in the silicate-free Na electrolyte (Fig. 6), in line with the results of earlier work on the effect of silicate on phosphate retention by iron oxidation products (Mayer and Jarrell, 2000). The reduced phosphate release in the Na+Si compared to the Na electrolyte can be attributed to the fact that silicate promotes the formation of ferrihydrite during Fe(II) oxidation in phosphate-depleted solutions (Voegelin et al., 2010; Voegelin et al., 2013; Senn et al., 2015). Ferrihydrite has a higher oxyanion sorption capacity than lepidocrocite formed in silicate-free background electrolytes and is therefore expected to more effectively retain phosphate released during Fe(III)-phosphate transformation. Calculations based on the LCF results and the $(P/Fe)_{ppt}$ confirmed that part of the phosphate released by Fe(III)-phosphate transformation in the Na+Si electrolyte was indeed taken up by the ferrihydrite ($(P/Fe)_{Fh-Si^*} \sim 0.09$; (Table EA7)).

In terms of structural transformation, the presence of ferrihydrite as an effective phosphate sink has been reported to promote Fe(III)-phosphate transformation into Fe(III)-(hydr)oxide (McLaughlin and Syers, 1978). The spectroscopic data however show that Fe(III)-phosphate transformation in the Na+Si electrolyte was markedly reduced compared to the Na electrolyte (Fig. 3). This stabilizing effect of silicate on Fe(III)-phosphate may be due to the intimate association of sequentially formed Fe(III)-phosphate and silicate-containing ferrihydrite within individual precipitate nanoparticles (Senn et al., 2015). Phosphate released by Fe(III)-phosphate

transformation may not readily displace silicate from ferrihydrite polymers due to the remaining high silicate concentration in solution, and the release of both phosphate and silicate into solution may be attenuated by slow intraparticle diffusion (Fuller et al., 1993a), which may in turn reduce the driving force for Fe(III)-phosphate transformation. The lower phosphate plateau concentration in the Na+Si than in the Na electrolyte (Fig. 6) may therefore not only be due to effective uptake of phosphate by ferrihydrite, but may also reflect the stabilizing effect of silicate on Fe(III)-phosphate formed in the Na+Si electrolyte.

By far the lowest extent of Ca-Fe(III)-phosphate transformation was observed in the Ca+Si electrolyte (Fig. 3). This can be attributed to the stabilization of Ca-Fe(III)-phosphate by Ca and possibly also by silicate and to the formation of ferrihydrite in the silicate-containing electrolyte, as described above for the Ca and Na+Si electrolytes. In addition, the stability of the bulk precipitates may be further enhanced by favorable electrostatic interactions or ternary complex formation between Ca and phosphate adsorbed on the ferrihydrite-type precipitate fraction (Antelo et al., 2015).

4.2.4. *No crystallization of amorphous (Ca-)Fe(III)-phosphate during aging*

Amorphous (Ca-)Fe(III)-phosphate may not only transform into Fe(III)-(hydr)oxide, with concomitant phosphate release, but also into crystalline (Ca-)Fe(III)-phosphate. Amorphous Fe(III)-phosphate precipitated at low pH transforms into crystalline Fe(III)-phosphate such as strengite over time (Roncal-Herrero et al., 2009), in analogy to the transformation of amorphous Fe(III)-arsenate into scorodite (Paktunc et al., 2008). Due to the neutral to slightly alkaline pH in our experiments, however, such a transformation was not observed. Alternatively, amorphous basic (Ca-)Fe(III)-phosphate formed at near-neutral pH may transform into a crystalline (Ca-)Fe(III)-phosphate, in analogy to the transformation of amorphous Ca-Fe(III)-arsenate into crystalline arseniosiderite at neutral pH and temperatures of 75-85 °C (Paktunc et al., 2015).

Mitridatite is a basic Ca-Fe(III)-phosphate isostructural to arseniosiderite (Moore and Araki, 1977), and Ca-Fe(III)-phosphate polymers with mitridatite-like local Fe(III)-coordination were observed in the fresh amorphous Ca-Fe(III)-phosphate precipitates formed in the Ca and Ca+Si electrolytes at high $(P/Fe)_{init}$ (Senn et al., 2015). However, XRD results did not reveal the formation of crystalline mitridatite during the aging of amorphous Ca-Fe(III)-phosphate for 30 days at 40 °C and the XAS results did not show an increase of the fraction of mitridatite-like polymers, suggesting that the crystallization of mitridatite requires higher temperatures and/or longer reaction times.

4.3. Ferrihydrite formation from (Ca-)Fe-phosphate in silicate-free electrolytes

For fresh precipitates formed in the silicate-free electrolytes at $(P/Fe)_{init}$ below the critical $(P/Fe)_{crit}$ for exclusive Fe(III)-phosphate formation, we previously found that initially formed Fe(III)-phosphate immediately started to transform into a phosphate-rich ferrihydrite-type precipitate with a $(P/Fe)_{ppt}$ of ~0.25 during continuing Fe(II) oxidation (Voegelin et al., 2013; Senn et al., 2015).

The structural analysis of corresponding aged precipitates clearly showed that this transformation continued during aging (Fig. 3), its extent depending on the type and concentration of interfering cations and oxyanions as discussed in the preceding section. The analysis of the Fe K-edge EXAFS data further suggested that the extent of corner-sharing Fe-Fe linkage in the ferrihydrite-type transformation product of Fe(III)-phosphate increased during aging (shift from HFO to Fh/HFO as proxy for ferrihydrite-type transformation product; see section 3.2.1). This increase in Fe-Fe coordination is indicative for a 3-dimensional growth of the ferrihydrite crystallites, and has previously been reported with respect to the aging of ferrihydrite-type Fe(III)-precipitates formed in the presence of arsenate (Waychunas et al., 1993; Paktunc et al., 2008). Previous work has shown that the increase of ferrihydrite crystallite size

results in a decreasing oxyanion sorption capacity (Fuller et al., 1993a; Waychunas et al., 1993). Indeed, linear regression analysis of the $(P/Fe)_{ppt}$ of precipitates formed at $(P/Fe)_{init}$ of ~ 0.2 - 0.75 in the silicate-free electrolytes Na, Mg and low Ca (Table EA7) indicates that the P/Fe of the ferrihydrite-type transformation product decreased from ~ 0.25 in the fresh precipitates to 0.14 ± 0.03 (s.d., $n=3$) in the aged precipitates. This $(P/Fe)_{ppt}$ was assumed to represent the maximum sorption capacity of the ferrihydrite-type precipitate fraction, because most of the precipitates considered for the regression analysis still contained at least some Fe(III)-phosphate (Fig. 3). The observed decrease of the phosphate sorption capacity closely compares to a decrease of the phosphate sorption capacity of ferrihydrite from 0.26 to 0.16 P/Fe within 56 days of aging at pH ~ 6 (Gerke, 1993) or from 0.45 P/Fe for freshly synthesized hydrous ferric oxide to 0.24 after 8.5 h and 0.18 P/Fe after 24 h of aging at pH 7.0 (Mao et al., 2012). A similar decrease in arsenate retention was furthermore observed in aging experiments with arsenate-rich ferrihydrite-type co-precipitates (Fuller et al., 1993a; Paktunc et al., 2008).

In previous work, microscopic analysis of a fresh precipitate formed at $(P/Fe)_{init}$ of 0.42 in Na electrolyte showed that lepidocrocite platelets that had formed after the depletion of dissolved phosphate were attached to the surface of spherical Fe(III)-phosphate particles (Fig. 6B in Kaegi et al. (2010)). Analysis of the aged precipitate Na 0.51 A by electron microscopy, on the other hand, suggested the lepidocrocite platelets became covered with nanometer-sized particles with rough surfaces (Fig. 5g,i). These morphological features suggest that the transformation from Fe(III)-phosphate to Fh/HFO at $(P/Fe)_{init} \sim 0.5$ proceeds to a significant extent via a dissolution-precipitation process that leads to the accumulation of a ferrihydrite-type precipitate on the Lp platelets.

4.4. Ferrihydrite-type precipitates in silicate-containing electrolytes

In the Na+Si and Ca+Si electrolytes with $(\text{Si/Fe})_{\text{init}} \sim 1$, the fresh precipitate formed in the absence of phosphate was identified as a silicate-containing ferrihydrite (Fh-Si*) with a molar Si/Fe ratio of ~ 0.1 and with less corner-sharing linkage and less FeO_6 octahedral distortion than in 2-line ferrihydrite synthesized by forced Fe(III) hydrolysis using standard protocols (Senn et al., 2015). Comparison of the spectra of the fresh and aged silicate-containing ferrihydrite revealed no significant changes in Fe coordination during aging (Fig. 1). This suggested that structural 0.1 Si/Fe and residual ~ 0.45 mM dissolved silicate effectively prevented further polymerization of the ferrihydrite or its transformation into a crystalline Fe(III)-(hydr)oxide during 30 days of aging at 40 °C, in line with laboratory studies on the effect of silicate on ferrihydrite transformation (Schwertmann and Taylor, 1972a; Vempati and Loeppert, 1989) and the persistence of silicate-containing ferrihydrites in environmental systems (Carlson and Schwertmann, 1981; Jessen et al., 2005; Cismasu et al., 2011; Voegelin et al., 2014).

In the Na+Si electrolyte, transformation of initially precipitated Fe(III)-phosphate into a ferrihydrite-type precipitate was observed during aging, although to a lesser extent than in the Na electrolyte (Fig. 3). Because the ferrihydrite-type transformation product could not be differentiated from the initially formed silicate-containing ferrihydrite, the reference spectrum Fh-Si* represented the initially formed silicate-containing ferrihydrite as well as the phosphate-containing ferrihydrite formed by Fe(III)-phosphate transformation (Fig. 3). Linear regression of precipitate P/Fe ratios versus LCF-derived structural fractions suggested that the Fh-Si* fraction in the aged precipitates in the Na+Si electrolyte contained ~ 0.09 P/Fe (Table EA7). The uptake of phosphate by ferrihydrite during Fe(III)-phosphate transformation probably also involved the displacement of initially co-precipitated silicate, but the available data did not allow to assess the importance of this effect.

4.5. Transformation of poorly-crystalline lepidocrocite

In the silicate-free Na, Mg, low Ca and Ca electrolytes in the absence of phosphate, the fresh precipitate has previously been identified as poorly crystalline lepidocrocite (Senn et al., 2015), in line with other work (van Genuchten et al., 2014b). Previous work has shown that the aging of lepidocrocite leads to its transformation into thermodynamically more stable goethite and/or to an increase in lepidocrocite crystallinity (Schwertmann and Taylor, 1972b; Schwertmann and Taylor, 1972a). The transformation of lepidocrocite into goethite has been postulated to proceed via a dissolution-precipitation mechanism that involves the formation and growth of goethite nuclei. Oxyanions such as silicate can effectively inhibit the formation of goethite nuclei, and thereby constrain lepidocrocite aging to the increase in crystallite size (Schwertmann and Taylor, 1972a).

Comparison of the EXAFS spectra of the fresh and aged poorly crystalline lepidocrocite formed in the silicate-free background electrolytes (with 0.014 As(V)/Fe) (Fig. 2 and Fig. EA6) and analysis of corresponding XRD patterns (Fig. EA10) indicated that aging for 30 days at 40 °C resulted in a slight increase in short-range and stacking order of the lepidocrocite crystallites, but not in lepidocrocite-to-goethite transformation. On the other hand, experiments in phosphate-free Na electrolyte without ~0.014 As(V)/Fe showed that about 80% of the initially formed poorly crystalline lepidocrocite transformed into goethite during aging (Fig. 4 and Fig. EA9). The As(V) present in the silicate- and phosphate-free treatments thus seemed to exert a similar effect as previously described for silicate, which inhibits the nucleation of goethite crystallites and thereby the transformation of lepidocrocite into goethite via a dissolution-reprecipitation mechanism (Schwertmann and Taylor, 1972a; Cornell and Schwertmann, 2003). Considering the similarity in the interactions of phosphate and arsenate with Fe, phosphate at a ratio of 0.014 P/Fe most probably inhibits lepidocrocite-to-goethite transformation in the same way as observed for 0.014 As(V)/Fe. Our results also show that the transformation of lepidocrocite into

goethite may also be inhibited by Ca and Mg, but do not allow to resolve the cause of this effect or the conditions under which it occurs.

4.6. Kinetics of precipitate transformation processes

In this study, we compared the structure and composition of aged and fresh precipitates to assess changes during aging, but did not follow precipitate transformation over time. However, some indications on the kinetics of the observed transformation processes may be gained by comparing our results with published data.

From a compilation of kinetic data on the transformation of hydrous ferric oxide into more crystalline phases at pH 6.0 and temperatures from 25 °C to 70 °C, Ford (2002) derived a regression equation that indicates an approximately 2-fold increase of the reaction rate coefficient per 10 °C increase in temperature. From half conversion times of 2-line ferrihydrite to goethite/hematite at pH 7.0 and temperatures of 3 °C and 21 °C reported by Schwertmann et al. (2004), on the other hand, an approximately 4-fold increase in the reaction rate coefficient per 10 °C increase in temperature can be derived. If the temperature dependence of the transformation reactions in our aging experiments falls into a similar range, aging at 40 °C probably proceeded about 3-8 times faster than at 25 °C (“room temperature”).

In a recent study, we investigated Fe(II) oxidation, precipitate formation and the onset of aging over a time period of 5 h at a $(P/Fe)_{init}$ of 0.3 (8 mM $NaHCO_3$; initial pH 6.3; 1 mM Fe_{tot} ; room temperature (Voegelin et al., 2013)). The data indicated that Fe(II) oxidation was complete after 2 h, and that about 2.5% of the total phosphate was released back into solution during the next 3 h (Fig. EA6 in Voegelin et al. (2013)). Assuming that the release of phosphate continued linearly over time, ~3.3 days would have been required to release 65% of the total phosphate into solution, i.e., to reach the level of phosphate release observed after the aging of the precipitate with the same $(P/Fe)_{init}$ of 0.3 in the current study (Fig. 6b; sample Na 0.3). Furthermore, results

from a similar experiment with a precipitate formed at $(P/Fe)_{init}$ of ~ 0.2 (with 0.1 mM Fe(II)) in 5 mM $NaHCO_3$ at pH 7.0 (Mayer and Jarrell, 2000) indicated that the decrease of $(P/Fe)_{ppt}$ from ~ 0.2 to ~ 0.05 (similar to the decrease in our experiment Na 0.2; see section 4.2.2) occurred within the first 5 days of aging. From these two comparisons, we thus conclude that the polymerization of Fe(III)-phosphate and phosphate-rich hydrous ferric oxide into phosphate-loaded ferrihydrite in the Na electrolyte was completed within the first part of the 30-days aging period.

In the experiment Na+Si 0.2 (with $(Si/Fe)_{init} \sim 1$ and $(P/Fe)_{init} \sim 0.2$), $\sim 55\%$ of the total phosphate were released back into solution after aging (Fig. 6f), corresponding to a decrease in $(P/Fe)_{ppt}$ from ~ 0.2 to ~ 0.09 . For a similar experiment with a precipitate formed at $(P/Fe)_{init} \sim 0.2$ and $(Si/Fe)_{init} \sim 3.6$ (5 mM $NaHCO_3$, pH 7.0; 0.1 mM Fe_{tot}), Mayer and Jarrell (2000) reported that only 10% of the total phosphate was released back into solution within 5 days. Assuming that phosphate release in their experiment continued linearly over time, $\sim 60\%$ phosphate release would have occurred over 30 days, qualitatively in line with the 55% release observed in our experiment. Noting that phosphate release after 30 days of aging of the precipitate Na+Si 0.3 approached the release in the respective experiment Na 0.3 without silicate (Fig. 6), it is probable that the initial phase of precipitate transformation and phosphate release in the Na+Si electrolyte was also nearly complete.

Compared to Fe(III)-phosphates formed in the Na electrolyte, Fe(III)-phosphate and Ca-Fe(III)-phosphate formed in the Mg, low Ca, Na+Si, Ca and Ca+Si electrolytes was markedly more resistant towards transformation during aging for 30 days at 40 °C (Fig. 3). Nevertheless, the phosphate plateau concentrations observed in the Mg, low Ca and Na+Si electrolytes at intermediate $(P/Fe)_{init}$ suggested that the initial transformation of (Ca-)Fe(III)-phosphate in these

suspensions was also fast and that further precipitate transformation within the 30-days aging period was inhibited by the release of phosphate.

For arsenate-sorbed hydrous ferric oxide with $(\text{As/Fe})_{\text{ppt}}$ of 0.07, crystallization (probed as decrease in 0.4 M HCl-extractable Fe) during aging at pH 6.0 and 40 °C has been reported to proceed with a half-life time of ~2.5 years, without formation of XRD-detectable amount of hematite or goethite within 125 days of aging (Ford, 2002). Similarly, no structural transformation of a ferrihydrite-type Fe(III)-As(V)-coprecipitate formed at pH 7.0 with an As/Fe ratio of 0.1 was observed during 210 days of aging and Fe remained completely oxalate-extractable (Violante et al., 2007).

Based on our results and the results from previous studies, we assume that the initial transformation of Fe(III)-phosphate and phosphate-saturated hydrous ferric oxide into a ferrihydrite-type precipitate with lower $(\text{P/Fe})_{\text{ppt}}$ was completed after the 30-days aging period examined in the present work, and that the transformation of phosphate- and (silicate-)sorbed ferrihydrite into more crystalline Fe(III)-(hydr)oxides will require substantially more time. To reliably determine the kinetics of the different transformation processes identified in this study, however, time-resolved experiments on the structural and compositional transformation of selected types of Fe(III)-precipitates are needed.

5. CONCLUSIONS

We have previously shown that the composition and structure of the iron oxidation products and their capacity to sequester phosphate depend on the concentrations of phosphate, silicate, Mg and Ca in solution (Senn et al., 2015). The present study emphasizes that these ions also critically affect the transformation of Fe(III)-precipitates during aging, as schematically summarized in Fig. 8.

With respect to the effects of oxyanions, this study shows that dissolved phosphate at sufficiently high concentration stabilizes Fe(III)-phosphate precipitates with low degree of Fe polymerization against transformation into ferrihydrite-type precipitates, and that silicate (and phosphate) stabilize ferrihydrite-type precipitates against transformation into a more crystalline Fe(III)-(oxyhydr)oxide within 30 days at 40 °C. The results also reveal that trace levels of arsenate (and probably in analogy phosphate) are sufficient to inhibit the transformation of lepidocrocite into goethite during aging.

Regarding the background electrolyte cations Na, Mg and Ca, our results demonstrate that bivalent cations, especially Ca and to a lesser extent Mg, strongly influence Fe(III)-precipitate transformation processes. In the case of amorphous Fe(III)-phosphate, specific (Ca) and electrostatic (Ca and Mg) interactions of Ca and Mg with phosphate lead to enhanced structural stability and reduced phosphate release during aging, an important aspect that has not been examined to date and warrants further consideration. In addition, our results indicate that, in the absence of interfering oxyanions, bivalent cations may also affect the transformation of lepidocrocite to goethite. More generally, this study demonstrates that the choice of background electrolyte may substantially affect the outcome of studies on the formation and transformation of Fe(III)-precipitates and that bivalent cations such as Mg or Ca should not be considered inert.

The transformation of Fe(III)-precipitates is associated with a loss of oxyanion retention capacity, resulting in the release of initially co-precipitated phosphate (Fig. 6 and Fig. 7). However, the fate of phosphate during aging is also affected by interactions with Ca and the formation of Ca-Fe(III)-phosphate and Ca-phosphate precipitates. Thus, even under conditions where phosphate uptake into fresh Fe(III)-precipitates does not represent a long-term phosphate sink due to Fe(III)-precipitate transformation, temporary phosphate storage in Fe(III)-precipitates

may allow slower processes such as Ca-phosphate precipitation to proceed and may thereby contribute to longer-term phosphate retention.

As shown in this study, the effects of individual solutes on Fe(III)-precipitate transformation and phosphate retention are interdependent and their coupled effects can only be resolved based on multifactorial experiments that account for the chemical conditions in specific types of environments. In addition to the effects of Ca, Mg, phosphate, silicate and arsenate addressed in this study, Fe(III)-precipitate formation and structure in natural environments may be further confounded by factors such as interactions with natural organic matter (Karlsson and Persson, 2010; Mikutta, 2011) or aluminum (Taylor and Schwertmann, 1978; Violante et al., 2009; Adra et al., 2013) or transformations triggered by sorbed Fe(II) (Pedersen et al., 2005; Boland et al., 2014), pointing to the need for further more comprehensive multifactorial experiments.

Via their effects on the structure, composition and aging of Fe(III)-precipitates, phosphate, silicate, Mg and Ca are expected to also critically influence the fate of co-transformed trace elements. The results from the present study thus emphasize the need to account for the structural complexity and dynamic properties of amorphous to poorly-crystalline Fe(III)-precipitates when addressing their role for trace element sequestration in natural and technical systems.

6. ACKNOWLEDGEMENTS

Irene Brunner, Thomas Rüttimann and Numa Pfenninger (Eawag, Switzerland) are acknowledged for assistance with laboratory experiments and analyses. The Angströmquelle Karlsruhe (ANKA, Karlsruhe, Germany) and the Swiss Norwegian Beamline (SNBL, ESRF, Grenoble, France) are acknowledged for providing synchrotron XAS beamtime. We thank Herman Emerich and Wouter van Beek (SNBL, ESRF) for their help during XAS data acquisition. The Scientific Center for Optical and Electron Microscopy of the ETH Zurich

(ScopeM) is acknowledged for access to electron microscopes. Two anonymous reviewers and Thilo Behrends are acknowledged for their constructive comments on an earlier version of this manuscript. This project was financially supported by the Swiss National Science Foundation under contracts No. 200021-132123 and 200020-152993.

7. REFERENCES

- Adra, A., Morin, G., Ona-Nguema, G., Menguy, N., Maillot, F., Casiot, C., Bruneel, O., Lebrun, S., Juillot, F., Brest, J. (2013). Arsenic Scavenging by Aluminum-Substituted Ferrihydrites in a Circumneutral pH River Impacted by Acid Mine Drainage. *Environmental Science & Technology* **47**, 12784-12792.
- Antelo, J., Arce, F., Fiol, S. (2015). Arsenate and phosphate adsorption on ferrihydrite nanoparticles. Synergetic interaction with calcium ions. *Chemical Geology* **410**, 53-62.
- Baken, S., Moens, C., van der Grift, B., Smolders, E. (2016). Phosphate binding by natural iron-rich colloids in streams. *Water Research* **98**, 326-333.
- Baken, S., Salaets, P., Desmet, N., Seuntjens, P., Vanlierde, E., Smolders, E. (2015). Oxidation of iron causes removal of phosphorus and arsenic from streamwater in groundwater-fed lowland catchments. *Environmental Science and Technology* **49**, 2886-2894.
- Boland, D.D., Collins, R.N., Miller, C.J., Glover, C.J., Waite, T.D. (2014). Effect of Solution and Solid-Phase Conditions on the Fe(II)-Accelerated Transformation of Ferrihydrite to Lepidocrocite and Goethite. *Environmental Science & Technology* **48**, 5477-5485.
- Borch, T., Kretzschmar, R., Kappler, A., Cappellen, P.V., Ginder-Vogel, M., Voegelin, A., Campbell, K. (2010). Biogeochemical Redox Processes and their Impact on Contaminant Dynamics. *Environmental Science & Technology* **44**, 15-23.
- Buffle, J., De Vitre, R.R., Perret, D., Leppard, G.G. (1989). Physico-chemical characteristics of a colloidal iron phosphate species formed at the oxic-anoxic interface of a eutrophic lake. *Geochimica et Cosmochimica Acta* **53**, 399-408.
- Carlson, L., Schwertmann, U. (1981). Natural ferrihydrites in surface deposits from Finland and their association with silica. *Geochimica et Cosmochimica Acta* **45**, 421-429.
- Châtellier, X., Grybos, M., Abdelmoula, M., Kemner, K.M., Leppard, G.G., Mustin, C., West, M.M., Paktunc, D. (2013). Immobilization of P by oxidation of Fe(II) ions leading to nanoparticle formation and aggregation. *Applied Geochemistry* **35**, 325-339.
- Cismasu, A.C., Michel, F.M., Tcaciuc, A.P., Brown Jr, G.E. (2014). Properties of impurity-bearing ferrihydrite III. Effects of Si on the structure of 2-line ferrihydrite. *Geochimica et Cosmochimica Acta* **133**, 168-185.
- Cismasu, A.C., Michel, F.M., Tcaciuc, A.P., Tylliszczak, T., Brown, J.G.E. (2011). Composition and structural aspects of naturally occurring ferrihydrite. *Comptes rendus Geoscience* **343**, 210-218.
- Cornell, R.M., Schwertmann, U. (2003) *The Iron Oxides: Structure, Properties, Reactions, Occurrences and Uses*. Wiley-VCH, Weinheim.
- Cumplido, J., Barrón, V., Torrent, J. (2000). Effect of Phosphate on the Formation of Nanophase Lepidocrocite from Fe(II) Sulfate. *Clays and Clay Minerals* **48**, 503-510.

- Deike, R.G., Granina, L., Callender, E., McGee, J.J. (1997). Formation of ferric iron crusts in Quaternary sediments of Lake Baikal, Russia, and implications for paleoclimate. *Marine Geology* **139**, 21-46.
- Doelsch, E., Rose, J., Masion, A., Bottero, J.Y., Nahon, D., Bertsch, P.M. (2000). Speciation and crystal chemistry of iron(III) chloride hydrolyzed in the presence of SiO₄ ligands. 1. An Fe K-edge EXAFS study. *Langmuir* **16**, 4726-4731.
- Feenstra, T.P., De Bruyn, P.L. (1979). Formation of calcium phosphates in moderately supersaturated solutions. *The Journal of Physical Chemistry* **83**, 475-479.
- Ford, R.G. (2002). Rates of hydrous ferric oxide crystallization and the influence on coprecipitated arsenic. *Environ. Sci. Technol.* **36**, 2459-2463.
- Frossard, E., Bauer, J.P., Lothe, F. (1997). Evidence of vivianite in FeSO₄-flocculated sludges. *Water Research* **31**, 2449-2454.
- Fuller, C.C., Davis, J.A., Waychunas, G.A. (1993a). Surface chemistry of ferrihydrite: Part 2. Kinetics of arsenate adsorption and coprecipitation. *Geochimica et Cosmochimica Acta* **57**, 2271-2282.
- Fuller, C.C., Davis, J.A., Waychunas, G.A. (1993b). Surface chemistry of ferrihydrite: Part 2. Kinetics of arsenate adsorption and coprecipitation. *Geochimica et Cosmochimica Acta* **57**, 2271-2282.
- Galvez, N., Barron, V., Torrent, J. (1999). Effect of phosphate on the crystallization of hematite, goethite, and lepidocrocite from ferrihydrite. *Clays and Clay Minerals* **47**, 304-311.
- Gerke, J. (1993). Phosphate adsorption by humic/Fe-oxide mixtures aged at pH 4 and 7 and by poorly ordered Fe-oxide. *Geoderma* **59**, 279-288.
- Griffioen, J. (2006). Extent of immobilisation of phosphate during aeration of nutrient-rich, anoxic groundwater. *Journal of Hydrology* **320**, 359-369.
- Gunnars, A., Blomqvist, S., Johansson, P., Andersson, C. (2002). Formation of Fe(III) oxyhydroxide colloids in freshwater and brackish seawater, with incorporation of phosphate and calcium. *Geochimica et Cosmochimica Acta* **66**, 745-758.
- Isaure, M., Laboudigue, A., Manceau, A., Sarret, G., Tiefert, C., Trocellier, P., Lambelle, G., Hazeman, J., Chateignier, D. (2002). Quantitative Zn speciation in a contaminated dredged sediment by μ -PIXE, μ -SXRF, EXAFS spectroscopy and principal component analysis. *Geochimica et Cosmochimica Acta* **66**, 1549-1567.
- Jessen, S., Larsen, F., Bender Koch, C., Arvin, E. (2005). Sorption and desorption of arsenic to ferrihydrite in a sand filter. *Environmental Science and Technology* **39**, 8045-8051.
- Kaegi, R., Voegelin, A., Folini, D., Hug, S.J. (2010). Effect of phosphate, silicate, and Ca on the morphology, structure and elemental composition of Fe(III)-precipitates formed in aerated Fe(II) and As(III) containing water. *Geochimica et Cosmochimica Acta* **74**, 5798-5816.
- Karlsson, T., Persson, P. (2010). Coordination chemistry and hydrolysis of Fe(III) in a peat humic acid studied by X-ray absorption spectroscopy. *Geochimica et Cosmochimica Acta* **74**, 30-40.
- Kellermeier, M., Glaab, F., Klein, R., Melero-Garcia, E., Kunz, W., Garcia-Ruiz, J.M. (2013). The effect of silica on polymorphic precipitation of calcium carbonate: an on-line energy-dispersive X-ray diffraction (EDXRD) study. *Nanoscale* **5**, 7054-7065.
- Majzlan, J., Lalinská, B., Chovan, M., Jurkovic, L., Milovská, S., Göttlicher, J. (2007). The formation, structure, and aging of As-rich hydrous ferric oxide at the abandoned Sb deposit Pezinok (Slovakia). *Geochimica et Cosmochimica Acta* **71**, 2007.

- Manceau, A., Marcus, M.A., Tamura, N. (2002) Quantitative speciation of heavy metals in soils and sediments by synchrotron X-ray techniques, in: Fenter, P.A., Rivers, M.L., Sturchio, N.C., Sutton, S.R. (Eds.), *Reviews in Mineralogy and Geochemistry*. Mineralogical Society of America, Washington, pp. 341-428.
- Mao, Y., Pham, A.N., Xin, Y., Waite, T.D. (2012). Effects of pH, floc age and organic compounds on the removal of phosphate by pre-polymerized hydrous ferric oxide. *Separation and Purification Technology* **91**, 38-45.
- Marcus, M.A., Macdowell, A.A., Celestre, R.S., Manceau, A., Miller, T., Padmore, H.A., Sublett, R.E. (2004). Beamline 10.3.2 at ALS: a hard X-ray microprobe for environmental and materials sciences. *Journal of Synchrotron Radiation* **11**, 239-247.
- Mayer, D.T., Jarrell, W.M. (1996). Formation and stability of iron(II) oxidation products under natural concentrations of dissolved silica. *Water Research* **30**, 1208-1214.
- Mayer, D.T., Jarrell, W.M. (2000). Phosphorus sorption during iron(II) oxidation in the presence of dissolved silica. *Water Research* **34**, 3949-3956.
- McLaughlin, J.R., Syers, J.K. (1978). Stability of ferric phosphates. *Journal of Soil Science* **29**, 499-504.
- Mikutta, C. (2011). X-ray absorption spectroscopy study on the effect of hydroxybenzoic acids on the formation and structure of ferrihydrite. *Geochimica et Cosmochimica Acta* **75**, 5122-5139.
- Moore, P.B., Araki, T. (1977). Mitridatite, $\text{Ca}_6(\text{H}_2\text{O})_6[\text{FeIII}_2\text{O}_6(\text{PO}_4)_4]\cdot 3\text{H}_2\text{O}$. A noteworthy octahedral sheet structure. *American Mineralogist* **16**, 1096-1106.
- Och, L.M., Müller, B., Voegelin, A., Ulrich, A., Göttlicher, J., Steiniger, R., Mangold, S., Vologina, E.G., Sturm, M. (2012). New insights into the formation and burial of Fe/Mn accumulations in Lake Baikal sediments. *Chemical Geology* **330-331**, 244-259.
- Paktunc, D., Dutrizac, J., Gertsman, V. (2008). Synthesis and phase transformations involving scorodite, ferric arsenate and arsenical ferrihydrite: Implications for arsenic mobility. *Geochimica et Cosmochimica Acta* **72**, 2649-2672.
- Paktunc, D., Majzlan, J., Huang, A., Thibault, Y., Johnson Michel, B., White Mary, A., 2015. Synthesis, characterization, and thermodynamics of arsenates forming in the Ca-Fe(III)-As(V)-NO₃ system: Implications for the stability of Ca-Fe arsenates, *American Mineralogist*, p. 1803.
- Parkhurst, D.L., Appelo, C.A.J. (1999) *User's guide to PHREEQC (Version 2) - a computer program for speciation, batch-reaction, one-dimensional transport, and inverse geochemical calculations*. U.S. Geological Survey, Denver, CO.
- Pedersen, H.D., Postma, D., Jakobsen, R., Larsen, O. (2005). Fast transformation of iron oxyhydroxides by the catalytic action of aqueous Fe(II). *Geochimica et Cosmochimica Acta* **69**, 3967-3977.
- Plant, L.J., House, W.A. (2002). Precipitation of calcite in the presence of inorganic phosphate. *Colloids and Surfaces A: Physicochemical and Engineering Aspects* **203**, 143-153.
- Ravel, B., Newville, M. (2005). ATHENA, ARTEMIS, HEPHAESTUS: data analysis for X-ray absorption spectroscopy using IFEFFIT. *Journal of Synchrotron Radiation* **12**, 537-541.
- Rea, B.A., Davis, J.A., Waychunas, G.A. (1994). Studies of the reactivity of the ferrihydrite surface by iron isotopic exchange and mössbauer spectroscopy. *Clays and Clay Minerals* **42**, 23-34.
- Roberts, L.C., Hug, S.J., Ruettimann, T., Billah, M.M., Khan, A.W., Rahman, M.T. (2004). Arsenic removal with iron(II) and iron(III) in waters with high silicate and phosphate concentrations. *Environmental Science and Technology* **38**, 307-315.

- Roncal-Herrero, T., Rodriguez-Blanco, J.D., Benning, L.G., Oelkers, E.H. (2009). Precipitation of iron and aluminum phosphates directly from aqueous solution as a function of temperature from 50 °C to 200 °C. *Crystal Growth & Design* **9**, 5197-5205.
- Rose, J., Manceau, A., Bottero, J.Y., Masion, A., Garcia, F. (1996). Nucleation and growth mechanisms of Fe oxyhydroxide in the presence of PO₄ ions. 1. Fe K-edge EXAFS study. *Langmuir* **12**, 6701-6707.
- Schwertmann, U., Carlson, L., Fechter, H. (1984). Iron oxide formation in artificial ground waters. *Schweizerische Zeitschrift für Hydrologie* **46**, 185-191.
- Schwertmann, U., Stanjek, H., Becher, H.-H. (2004). Long-term in vitro transformation of 2-line ferrihydrite to goethite/hematite at 4, 10, 15 and 25 °C. *Clay Minerals* **39**, 433-438.
- Schwertmann, U., Taylor, R.M. (1972a). The influence of silicate on the transformation of lepidocrocite to goethite. *Clays and Clay Minerals* **20**, 159-164.
- Schwertmann, U., Taylor, R.M. (1972b). The transformation of lepidocrocite to goethite. *Clays and Clay Minerals* **20**, 151-158.
- Senn, A.-C., Kaegi, R., Hug, S.J., Hering, J.G., Mangold, S., Voegelin, A. (2015). Composition and structure of Fe(III)-precipitates formed by Fe(II) oxidation in water at near-neutral pH: Interdependent effects of phosphate, silicate and Ca. *Geochimica et Cosmochimica Acta* **162**, 220-246.
- Stumm, W., Sulzberger, B. (1992). The cycling of iron in natural environments: Considerations based on laboratory studies of heterogeneous redox processes. *Geochimica et Cosmochimica Acta* **56**, 3233-3257.
- Taylor, K.G., Konhauser, K.O. (2011). Iron in Earth surface systems: A major player in chemical and biological processes. *Elements Magazine* **7**, 83-88.
- Taylor, R.M., Schwertmann, U. (1978). The Influence of Aluminum on Iron Oxides. Part I. The Influence of Al on Fe Oxide Formation from the Fe(II) System. *Clays and Clay Minerals* **26**, 373-383.
- Tessenow, U. (1974). Lösungs-, Diffusions- und Sorptionsprozesse in der Oberschicht von Seesedimenten. IV. Reaktionsmechanismen und Gleichgewichte im System Eisen-Mangan-Phosphat im Hinblick auf die Vivianitakkumulation im Ursee. *Archiv für Hydrobiologie Supplement* **47**, 1-79.
- Tung, M.S., Eidelma, N., Sieck, B., Brown, W.E. (1988). Octacalcium phosphate solubility product from 4 to 37 °C. *Journal of Research of the National Bureau of Standards*. **93**, 613-624.
- van der Grift, B., Behrends, T., Osté, L.A., Schot, P.P., Wassen, M.J., Griffioen, J. (2016). Fe hydroxyphosphate precipitation and Fe(II) oxidation kinetics upon aeration of Fe(II) and phosphate-containing synthetic and natural solutions. *Geochimica et Cosmochimica Acta* **186**, 71-90.
- van Genuchten, C.M., Gadgil, A.J., Peña, J. (2014a). Fe(III) nucleation in the presence of bivalent cations and oxyanions leads to subnanoscale 7 Å polymers. *Environmental Science and Technology* **48**, 11828-11836.
- van Genuchten, C.M., Peña, J., Amrose, S.E., Gadgil, A.J. (2014b). Structure of Fe(III) precipitates generated by the electrolytic dissolution of Fe(0) in the presence of groundwater ions. *Geochimica et Cosmochimica Acta* **127**, 285-304.
- Vempati, R.K., Loeppert, R.H. (1989). Influence of structural and adsorbed Si on the transformation of synthetic ferrihydrite. *Clays and Clay Minerals* **37**, 273-279.

- Violante, A., Gaudio, S.D., Pigna, M., Ricciardella, M., Banerjee, D. (2007). Coprecipitation of Arsenate with Metal Oxides. 2. Nature, Mineralogy, and Reactivity of Iron(III) Precipitates. *Environmental Science & Technology* **41**, 8275-8280.
- Violante, A., Pigna, M., Del Gaudio, S., Cozzolino, V., Banerjee, D. (2009). Coprecipitation of Arsenate with Metal Oxides. 3. Nature, Mineralogy, and Reactivity of Iron(III)–Aluminum Precipitates. *Environmental Science & Technology* **43**, 1515-1521.
- Voegelin, A., Kaegi, R., Berg, M., Nitzsche, K.S., Kappler, A., Lan, V.M., Trang, P.T.K., Göttlicher, J., Steininger, R. (2014). Solid-phase characterization of an effective household sand filter for As, Fe and Mn removal from groundwater in Vietnam. *Environmental Chemistry* **11**, 566–578.
- Voegelin, A., Kaegi, R., Frommer, J., Vantelon, D., Hug, S.J. (2010). Effect of phosphate, silicate, and Ca on Fe(III)-precipitates formed in aerated Fe(II)- and As(III)-containing water studied by X-ray absorption spectroscopy. *Geochimica et Cosmochimica Acta* **74**, 164-186.
- Voegelin, A., Senn, A.-C., Kaegi, R., Hug, S.J., Mangold, S. (2013). Dynamic Fe-precipitate formation induced by Fe(II) oxidation in aerated phosphate-containing water. *Geochimica et Cosmochimica Acta* **117**, 216-231.
- Waychunas, G.A., Rea, B.A., Fuller, C.C., Davis, J.A. (1993). Surface chemistry of ferrihydrite: Part 1. EXAFS studies of the geometry of coprecipitated and adsorbed arsenate. *Geochimica et Cosmochimica Acta* **57**, 2251-2269.

8. FIGURES

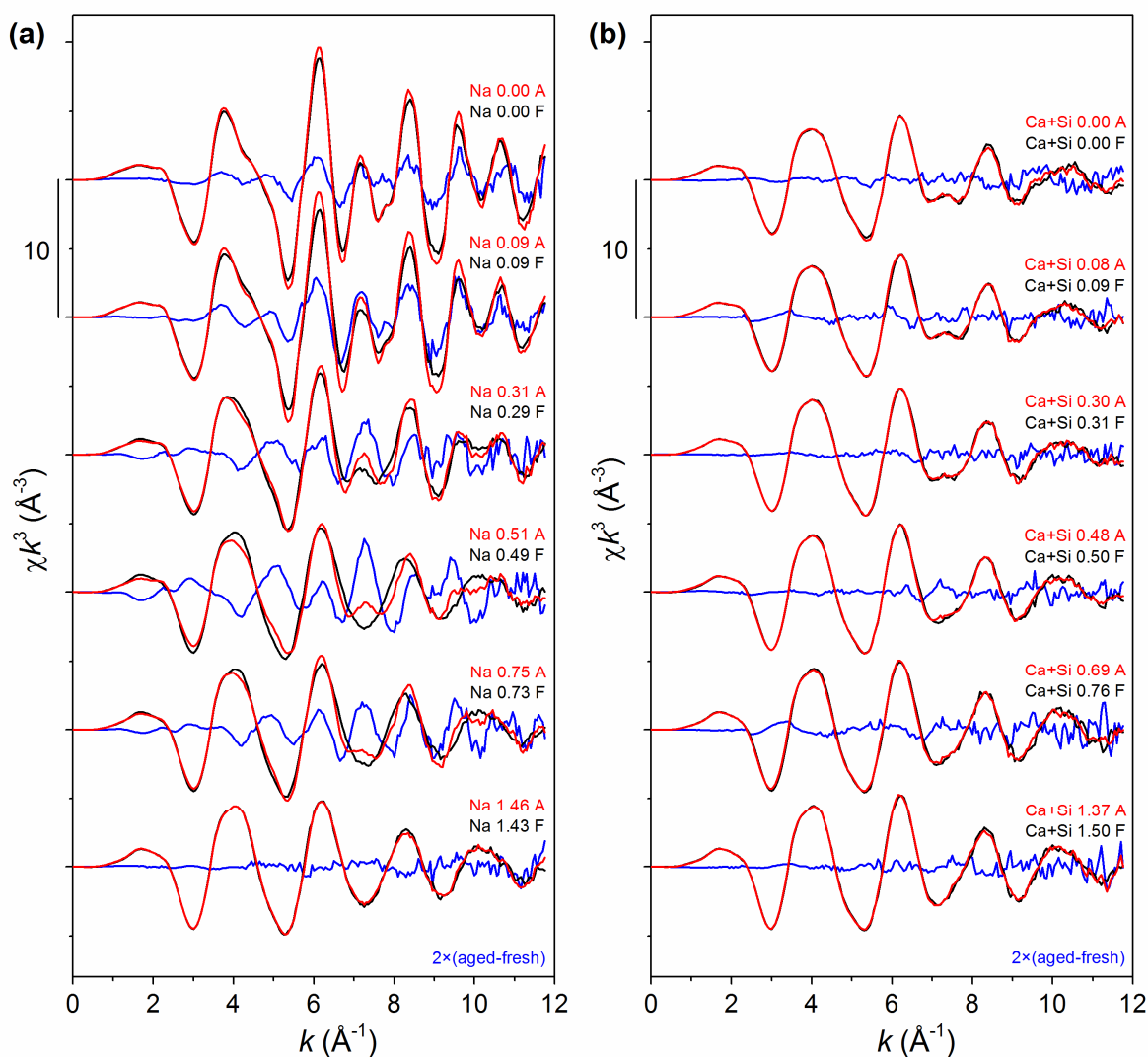


Fig. 1. Comparison of the Fe K-edge EXAFS spectra of aged (red lines) and fresh (black lines, from Senn et al. (2015)) precipitates formed in the Na (a) and Ca+Si (b) electrolytes at selected $(P/Fe)_{\text{init}}$. Difference spectra “aged – fresh” (blue lines, scaled by a factor of 2 to increase visibility) are shown to illustrate differences between the spectra of aged and fresh precipitates. Sample labels defined in the text.

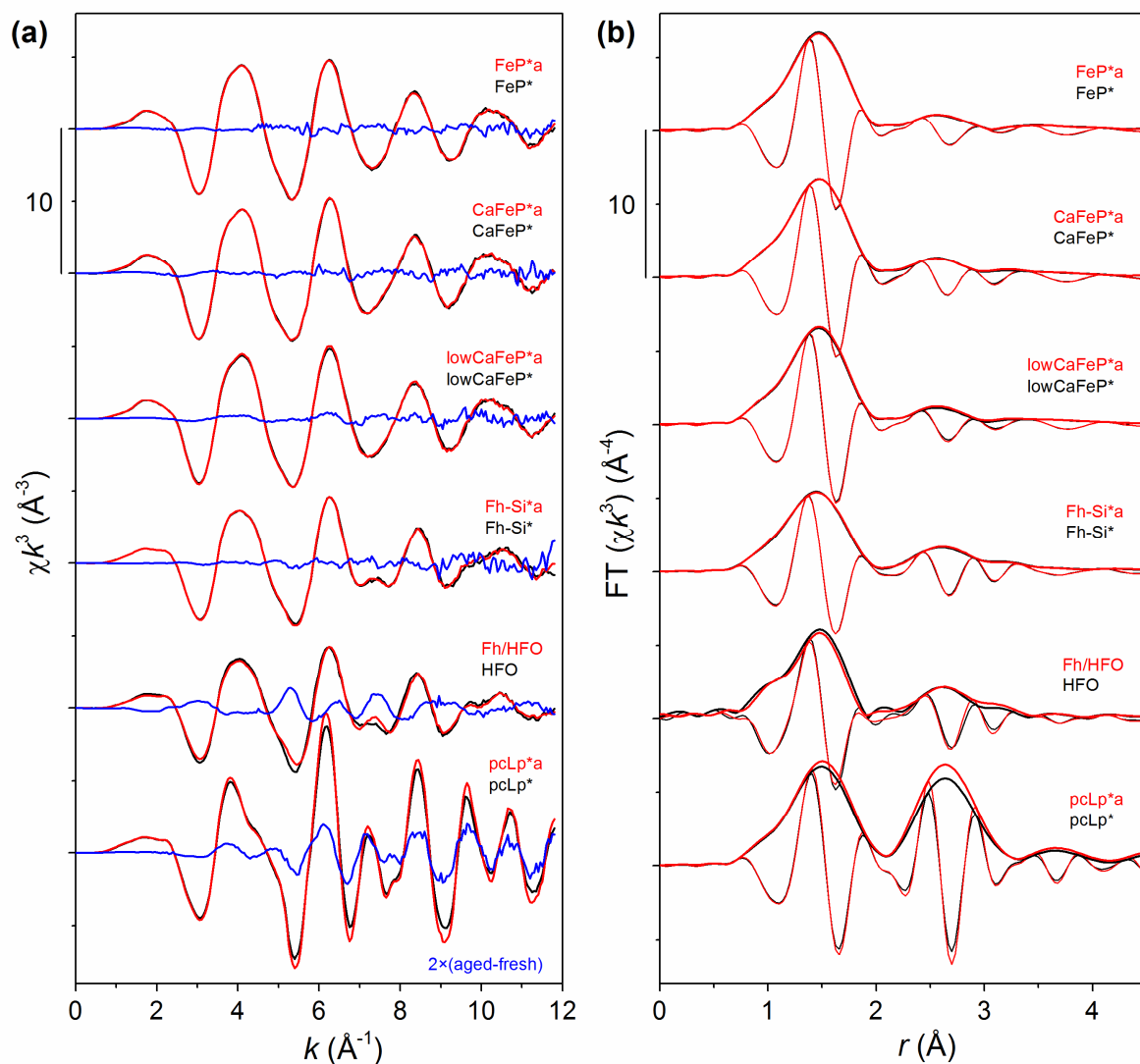


Fig. 2. Comparison of the Fe K-edge EXAFS spectra of aged (red lines) and fresh (black lines, from Senn et al. (2015)) endmember Fe(III)-precipitates in (a) k -space and (b) r -space. Difference spectra "aged - fresh" are shown in panel (a) (blue lines; scaled by a factor of 2 to increase visibility). The magnitudes (thick lines) and imaginary parts (thin lines) of the Fourier-transformed spectra are shown in panel (b). Sample labels defined in the text.

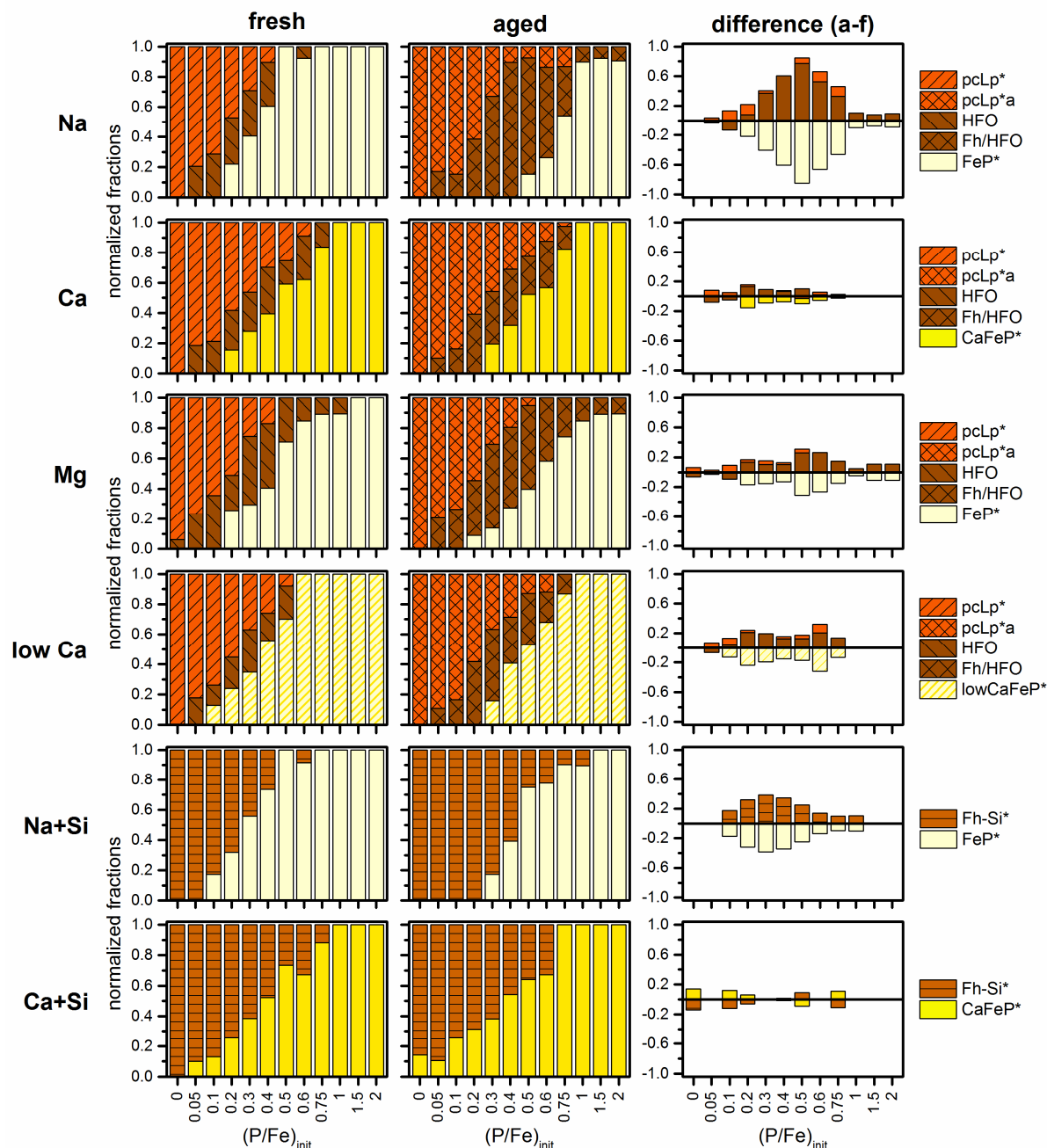


Fig. 3. Results from LCF analysis of the Fe K-edge EXAFS spectra of fresh and aged precipitates (results for fresh precipitates from Senn et al. (2015)) and their difference (aged minus fresh, differences pcLp*a-pcLp* and Fh/HFO-HFO shown without hatching). The reference spectra used for LCF analysis are shown in Fig. 2. Detailed fit results are listed in Table EA4. Statistical fit uncertainties were typically (90th percentile) <0.01 (pcLp*a), <0.03 (Fh-Si*, Fh/HFO) and <0.02 (FeP*, CaFeP* and lowCaFeP*) (further details in Table EA5). Sample labels defined in the text.

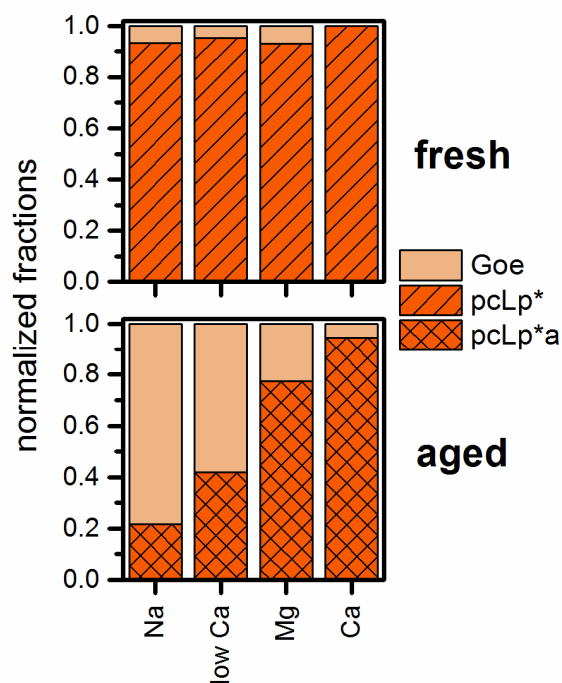


Fig. 4. Results of the LCF analysis of spectra of fresh and aged precipitates formed in phosphate- and silicate-free Na, low Ca, Mg and Ca electrolytes without arsenate. Experimental and reconstructed LCF spectra are shown in Fig. EA9, the complete LCF results are listed in Table EA6.

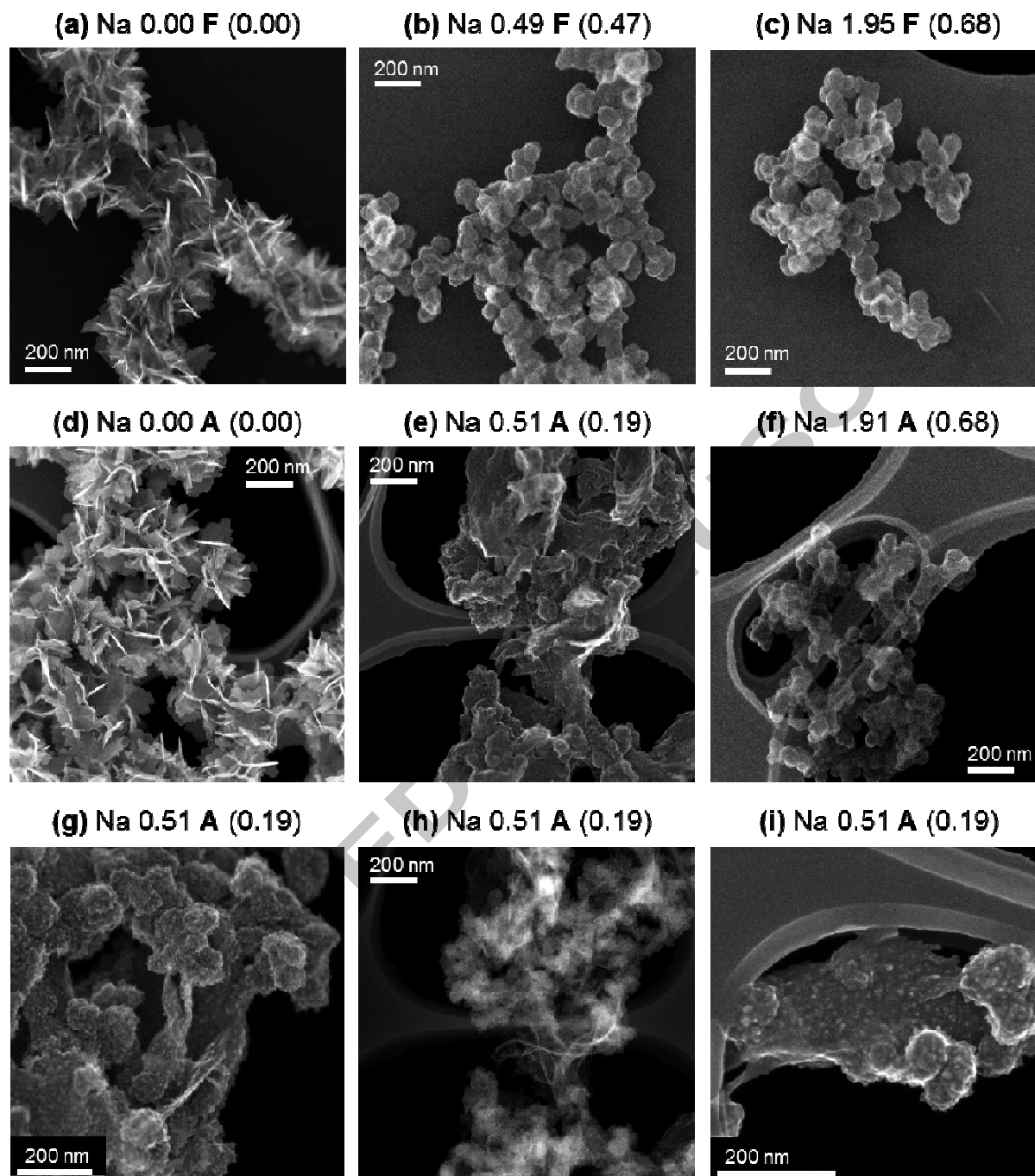


Fig. 5. Secondary electron (SE) images indicating the morphology of fresh (a-c) and aged (d-f) Fe(III)-precipitates formed in Na electrolyte at different $(P/Fe)_{init}$ ($(P/Fe)_{ppt}$ in parentheses). Corresponding high-angle annular dark-field (HAADF) image for Na 0.51 A (h) and SE images at higher resolution (g, i). HAADF images corresponding to SE images a-f are shown in Fig. EA11. SE images for precipitates formed in Ca electrolyte are shown in Fig. EA12.

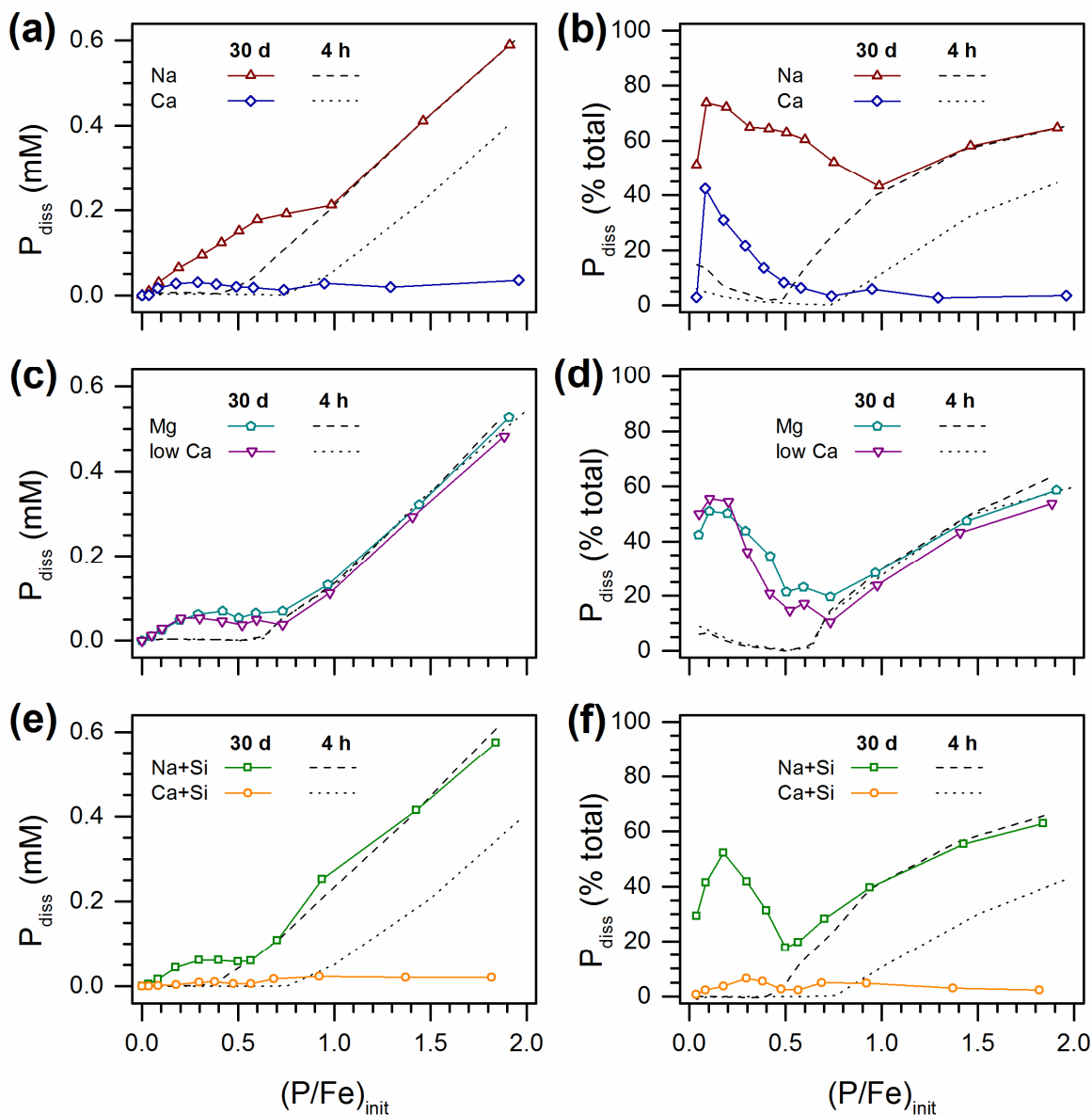


Fig. 6. Total dissolved phosphate (a,c,e) and fractions of dissolved phosphate (b,d,f) in the precipitate suspensions after aging for 30 days as a function of molar initial dissolved P/Fe ratio ($(P/Fe)_{\text{init}}$) in Na and Ca (a,b), low Ca and Mg (c,d) and Na+Si and Ca+Si (e,f) background electrolytes. For comparison, dashed and dotted lines show the respective data for fresh precipitate suspensions (Senn et al., 2015).

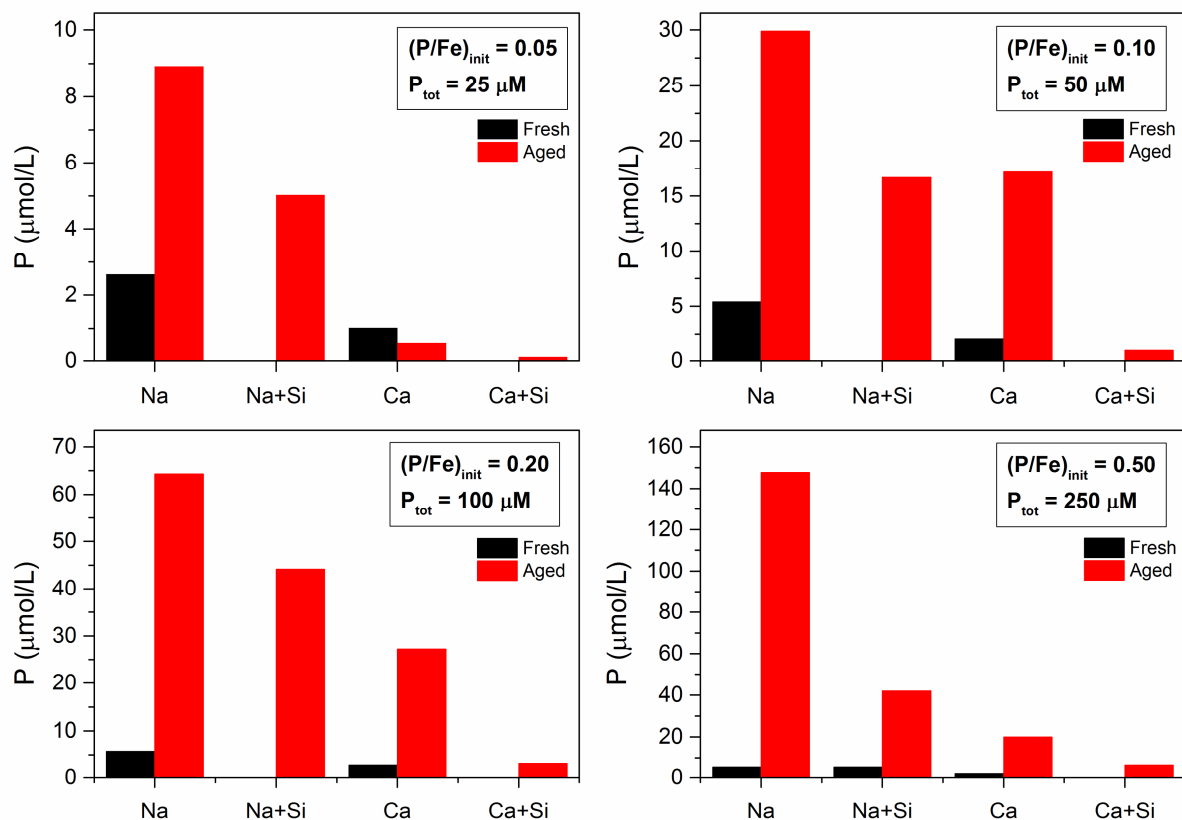


Fig. 7. Dissolved phosphate concentrations in fresh (Senn et al., 2015) and aged precipitate suspensions at (nominal) $(\text{P/Fe})_{\text{init}}$ of 0.05, 0.1, 0.2 and 0.5 in Na, Na+Si, Ca, and Ca+Si background electrolyte.

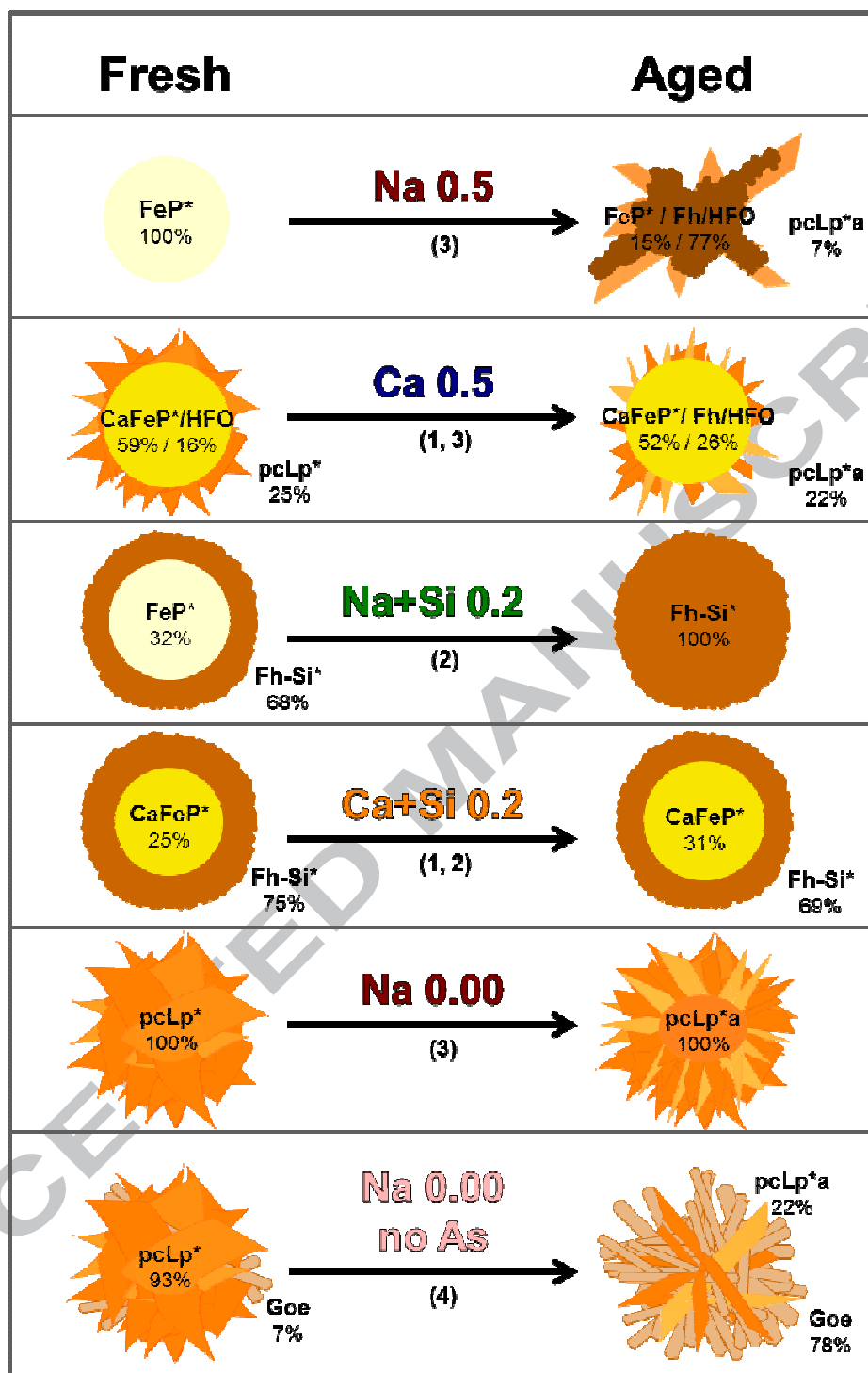


Fig. 8. Schematic representation of key effects of phosphate, silicate, Ca and arsenate on structural changes in Fe(III)-precipitates during aging. (1) Stabilization of CaFeP* phosphate by Ca against transformation into Fh/HFO during aging. (2) Induction of Fh-Si* formation in silicate-containing electrolytes with limited transformation during aging. (3) Growth of Lp crystallites during aging in 0.014 As(V)/Fe-containing suspensions and (4) partial transformation of poorly crystalline Lp into Goethite in absence of As(V). Concomitant changes in dissolved phosphate concentrations are shown in Figures 6 and 7.

Effect of aging on the structure and composition of Fe(III)-precipitates formed by Fe(II) oxidation in water

Anna-Caterina Senn^{a,b}, Ralf Kaegi^a, Stephan J. Hug^a, Janet G. Hering^{a,b,c},

Stefan Mangold^d, Andreas Voegelin^{a,}*

^a Eawag, Swiss Federal Institute of Aquatic Science and Technology, Ueberlandstrasse 133, CH-8600 Duebendorf, Switzerland

^b Department of Environmental Sciences, Institute of Biogeochemistry and Pollutant Dynamics, ETH, Swiss Federal Institute of Technology, Zurich, Switzerland

^c School of Architecture Civil and Environmental Engineering, EPFL, École Polytechnique Fédérale de Lausanne, Switzerland

^d Karlsruhe Institute of Technology, Institute of Synchrotron Radiation, Hermann-von-Helmholtz Platz 1, D-76344 Eggenstein-Leopoldshafen, Germany

* Corresponding author. E-mail address: andreas.voegelin@eawag.ch, phone +41 58 765 54 70, fax +41 58765 52 10

CONTENT (22 pages, 8 tables, 12 figures)

EA1. Experimental treatments and analytical methods used	2
EA2. Aged suspensions: pH values, element recoveries and replicate data	3
EA3. Fe K-edge EXAFS data	5
EA4. X-ray diffraction data	18
EA5. Additional scanning TEM images	20
EA6. Molar (P/Fe)_{ppt} ratios of precipitate fractions from linear regressions	21
EA7. Saturation indices of Ca-phosphates in low Ca and Ca electrolytes	21
EA8. References	22

EA1. Experimental treatments and analytical methods used

Table EA1. Overview over combinations of background electrolytes and P/Fe ratios studied and analytical techniques used for solution analysis and precipitate characterization^a.

Series ^b	(P/Fe) _{init} ^c (with Fe = 0.5 mM)											
	0.0	0.05	0.1	0.2	0.3	0.4	0.5	0.6	0.75	1.0	1.5	2.0
Na	IKSX	IK	IK	IK	IK	IK	IKSX	IK	IK	IK	IKX	IKS
Ca	IKSX	IK	IK	IK	IK	IK	IKSX	IK	IK	IK	IKX	IKS
Mg	IK	IK	IK	IK	IK	IK	IK	IK	IK	IK	IK	IK
low Ca	IK	IK	IK	IK	IK	IK	IK	IK	IK	IK	IK	IK
Na+Si	IK	IK	IK	IK	IK	IK	IK	IK	IK	IK	IK	IK
Ca+Si	IK	IK	IK	IK	IK	IK	IK	IK	IK	IK	IK	IK

^a For each of the 72 combinations, the initial and final suspensions were analyzed by ICP-MS (unfiltered/filtered) (I), and the corresponding precipitates by Fe K-edge EXAFS (K) spectroscopy. Selected precipitates were studied by STEM (S) and XRD (X).

^b *Na*: 8 mM NaHCO₃; *Ca*: 4mM Ca(HCO₃)₂; *low Ca*: 7 mM NaHCO₃ + 0.5 mM Ca(HCO₃)₂; *Mg*: 4 mM Mg(HCO₃)₂; *Na+Si*: 8 mM NaHCO₃ + 0.5 mM Na₂SiO₃; *Ca+Si*: 4 mM Ca(HCO₃)₂ + 0.5 mM Na₂SiO₃. Ca(HCO₃)₂ and Mg(HCO₃)₂ refer to CaCO₃ and MgO dissolved in CO₂-saturated water.

^c Molar phosphate/Fe(II) ratio in the starting solution.

EA2. Aged suspensions: pH values, element recoveries and replicate data

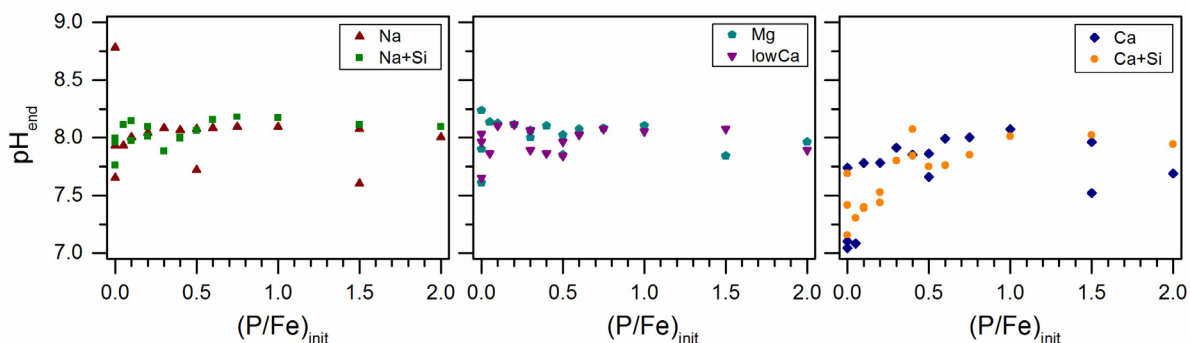


Fig. EA1. Final pH values (pH_{end}) of the reaction suspensions after 30 days reaction time for the six different background electrolytes.

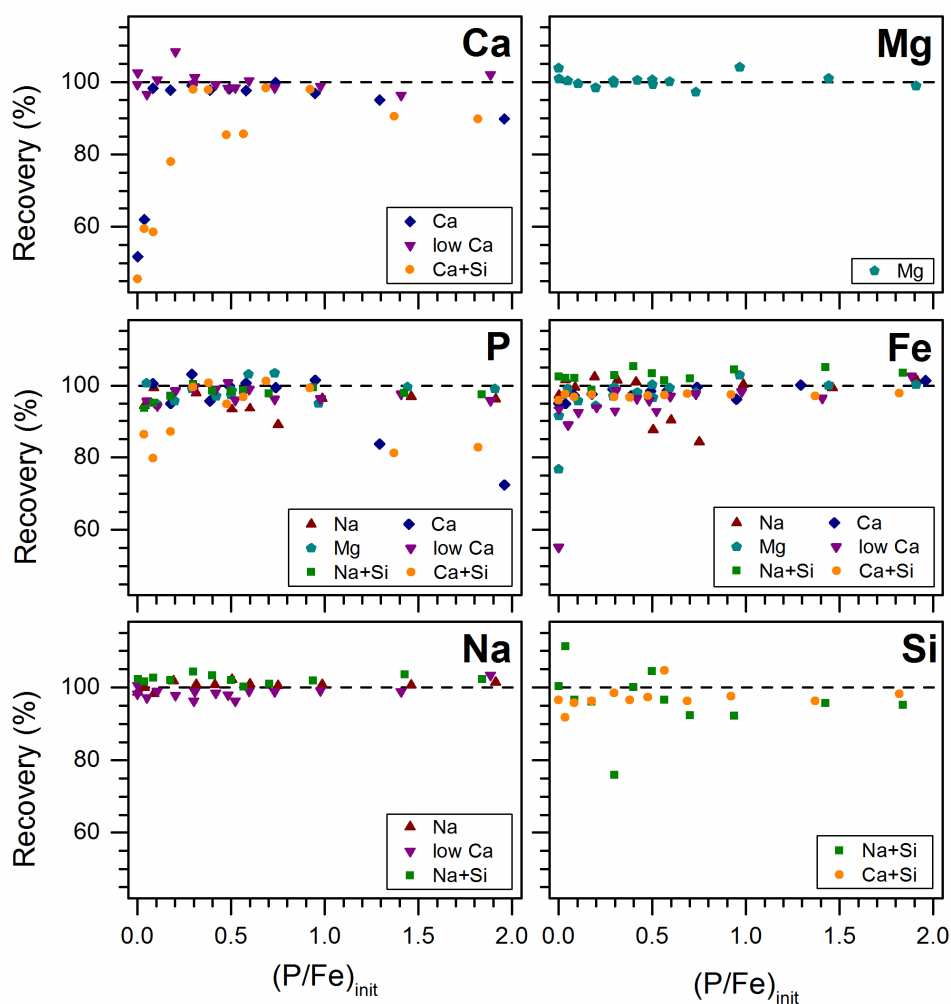


Fig. EA2. Total element recoveries in the reaction suspensions after 30 days reaction times for the six different background electrolytes. Calculated by dividing total Ca, Mg, P, Fe, Na and Si concentrations after 30 days ($[\text{unfilt}]_{\text{end}}$) by total initial Ca, Mg, P, Fe, Na and Si concentrations ($[\text{unfilt}]_{\text{init}}$), measured by ICP-MS.

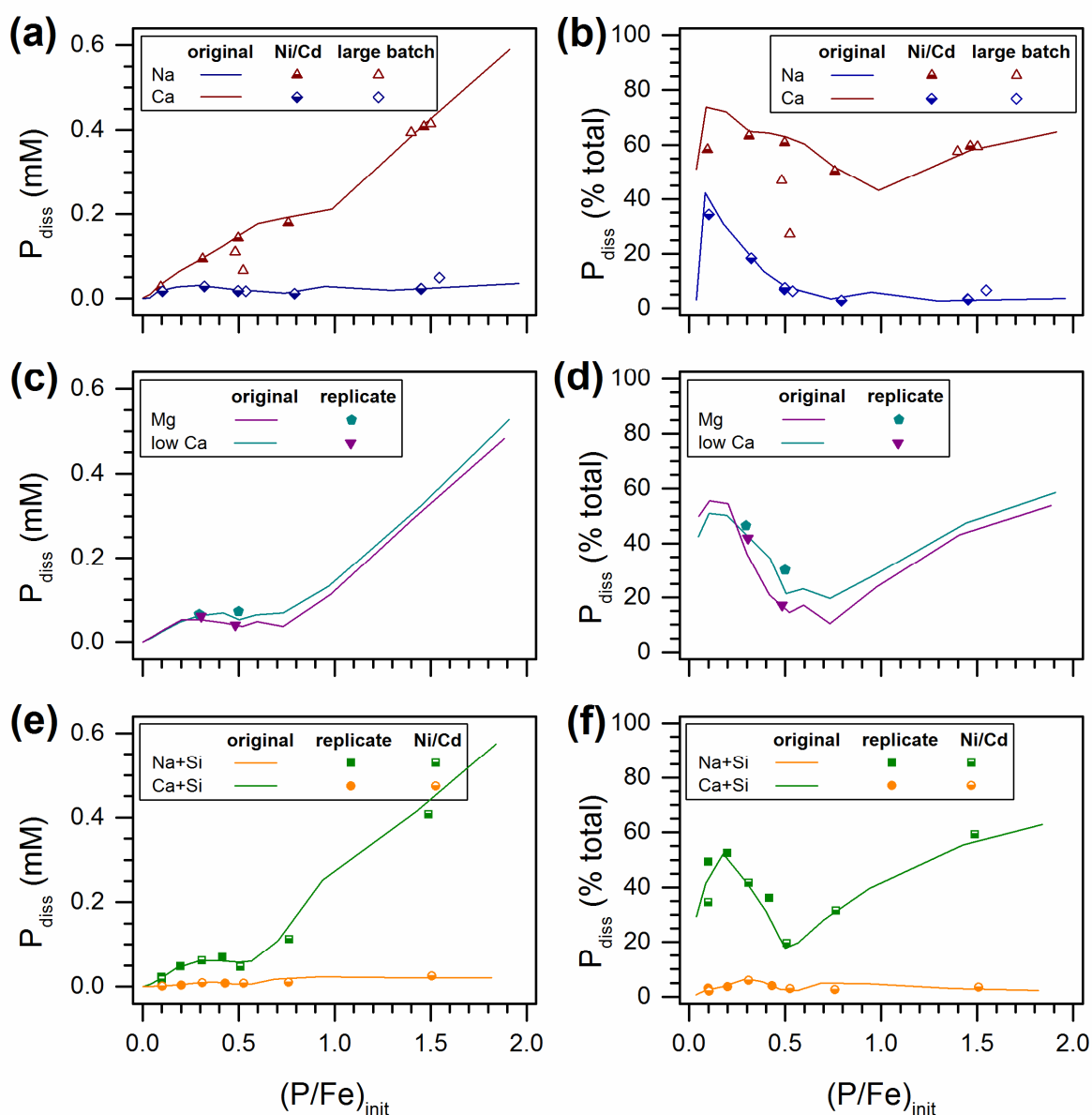


Fig. EA3. Dissolved phosphate in aging experiments (symbols) similar to the original experiment in comparison to the data shown in Fig. 6 (solid lines). Full symbols denote true replicates, half-filled symbols denote experiments in which 7 μM Ni and 7 μM Cd instead of 7 μM As(V) were added to the initial solutions under otherwise identical conditions. The open symbols denote experiments conducted in larger reaction vessels and with larger suspension volumes to collect more sample material for further analyses. In general, dissolved phosphate concentrations in these experiments, conducted over the course of 3 years with different calibration standards, agreed very well with the data from the original dataset. A substantial deviation from the original experiments was only observed in one experiment conducted with Na electrolyte at $(P/Fe)_{\text{init}}$ of 0.5 using a larger reaction vessel. The cause of this discrepancy could not be identified.

EA3. Fe K-edge EXAFS data

Principal component analysis and target testing

For principal component analysis (PCA) and target testing (TT) (Isaure et al., 2002; Manceau et al., 2002), software from beamline 10.3.2 at the Advanced Light Source (ALS, Berkely, USA) was used (Marcus et al., 2004). The k^3 -weighted Fe K-edge EXAFS spectra of all 72 aged precipitates were analyzed by PCA over the k -range 2-11 \AA^{-1} . Based on visual examination, the first four components were considered to represent the dominant spectral features (Fig. EA4a). Target testing revealed that these four spectral components allowed to adequately reproduce the first four PCA-components previously derived from the respective 72 spectra of fresh Fe(III)-precipitates (from Senn et al. (2015)) (Fig. EA4b). This close match suggested that nearly the same set of spectral components could be used to describe spectra collected on aged and fresh precipitates.

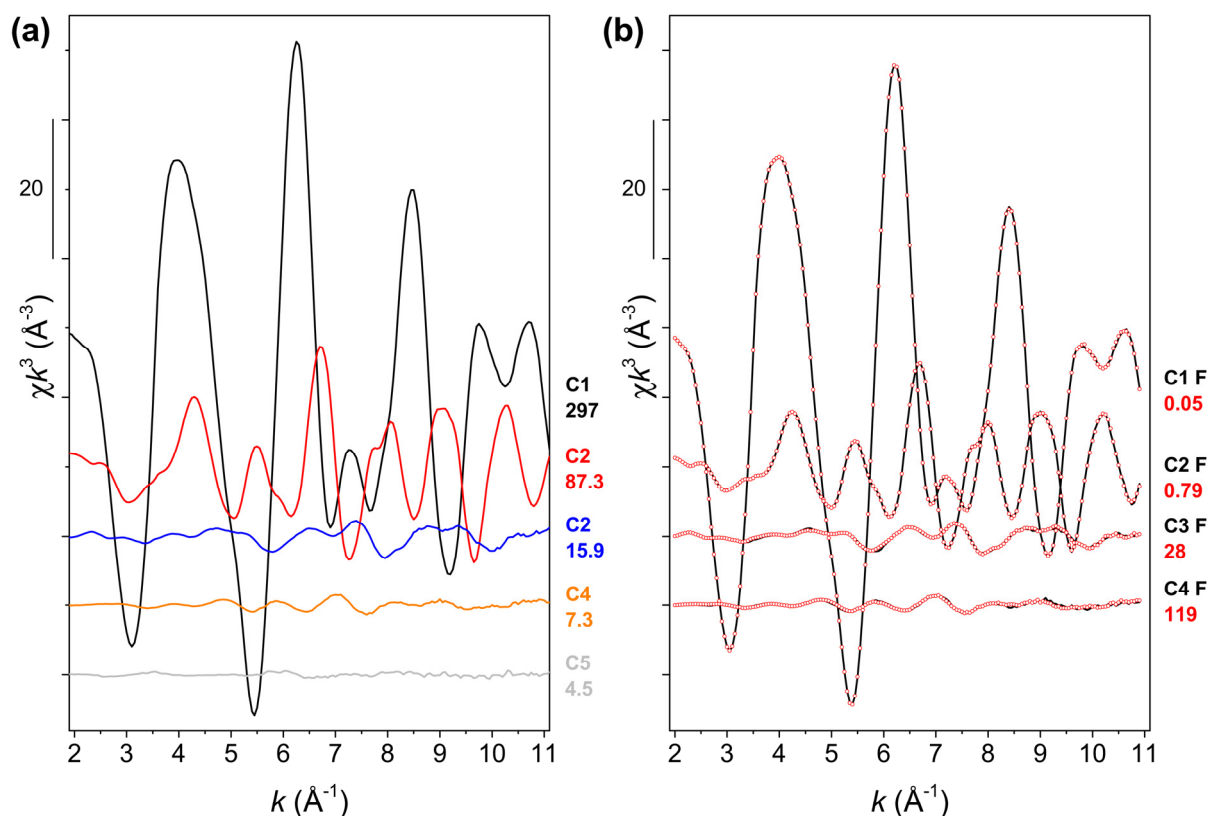


Fig. EA4. (a) First 5 components from PCA of all 72 Fe K-edge EXAFS spectra of aged precipitates over k -range 2-11 \AA^{-1} (numbers below component labels indicate Eigenvalue). (b) Target transforms (red dotted lines) of principal components C1 F to C4 F (black solid lines) derived from the 72 Fe K-edge EXAFS spectra of fresh precipitates based on components C1 to C4 derived from the spectra of aged precipitates (numbers below reference labels indicate NSSR×1000 of the target transform).

Grouped spectra

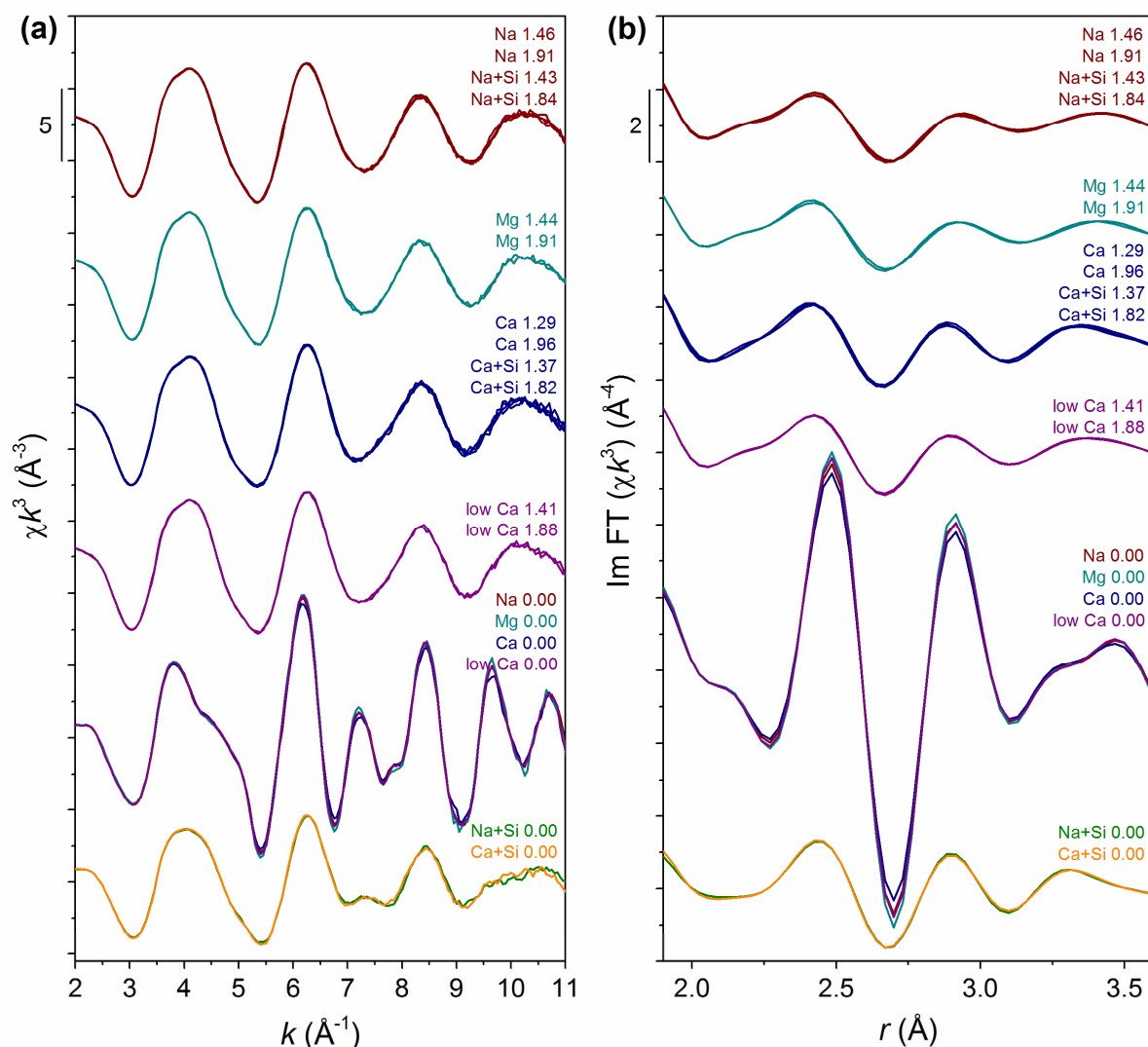


Fig. EA5. Comparison of Fe K-edge EXAFS spectra of aged precipitates formed at (P/Fe)_{init} of ~1.5 and ~2 in the Na and Na+Si electrolytes, Mg electrolyte, Ca and Ca+Si electrolytes, and low Ca electrolyte as well as of the spectra formed at (P/Fe)_{init} of 0.00 in absence (Na, Mg, Ca, and low Ca electrolytes) and presence of silicate (Na+Si and Ca+Si electrolytes). (a) Spectra in k -space. (b) Imaginary parts of Fourier-transformed spectra in r -space. The grouped spectra exhibited a very high similarity and were averaged to obtain (from top) the spectra FeP*a, MgFeP*a, CaFeP*a, lowCaFeP*a, pcLp*a and Fh-Si*a (shown in Fig. 2).

Comparison of the spectra of Lp, pcLp* and pcLp*a

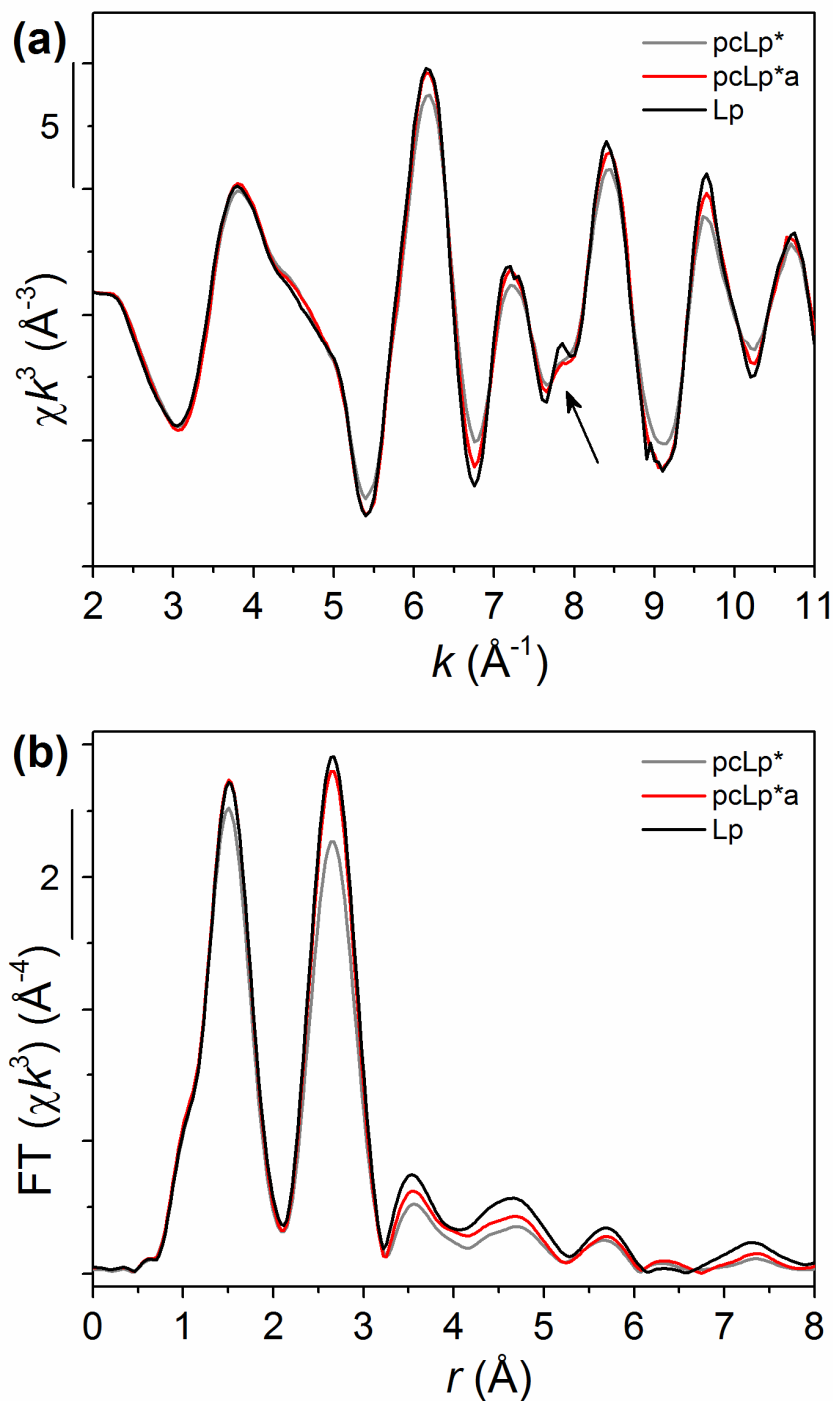


Fig. EA6. Comparison of the Fe K-edge EXAFS spectra of synthetic lepidocrocite (Lp), pcLp* and pcLp*aged. (a) Spectra in k -space. (b) Fourier-transformed spectra in r -space. The second-shell amplitude of the spectrum pcLp*a is nearly as high as in crystalline lepidocrocite. However, the amplitudes of more distant peaks are still markedly reduced, and the comparison of the spectra in k -space reveals that the spectrum pcLp*a lacks the (higher-frequency) feature visible in the spectrum Lp at about 7.8 \AA^{-1} (arrow). These differences suggest that the samples represented by the spectrum pcLp*a contained poorly crystalline Lp with less ordered local Fe coordination than in crystalline Lp.

PCA-TT and LCF analysis of spectra of precipitates from aged Na suspensions

Principal component analysis of the 12 spectra of aged precipitates formed in Na electrolyte returned a minimum for the empirical IND value (Manceau et al., 2002) for the third component, suggesting that three spectral components could explain the dataset. Target testing of reference spectra using the first three principal components returned empirical SPOIL values (Manceau et al., 2002) of 1.1 for pcLp*a, 0.9 for FeP*, 2.0 for Fh, 2.1 for Fh/HFO and 4.8 for the HFO reference spectrum. These results suggested that, in addition to the endmember spectra pcLp*a and FeP*, the spectra Fh and Fh/HFO were well-suited for LCF analysis, whereas the HFO reference spectrum was classified as poor reference. In Table EA2, LCF results are listed for the aged samples formed at (ideal) $(P/Fe)_{init}$ from 0.05 to 1.0 in Na electrolyte. To represent the ferrihydrite-type precipitate fraction, either the HFO, Fh/HFO or Fh reference spectrum was used. The normalized sums of the squared residuals (NSSR) or the individual fits confirm that the Fh/HFO and Fh references are significantly better suited to describe the ferrihydrite-type precipitate fraction than the HFO reference, in line with the results from target testing (on average, fits with Fh/HFO had a 26% lower NSSR and fits with Fh a 21% lower NSSR than fits with HFO, Table EA2). Comparison of the fits obtained with the Fh/HFO spectrum and the Fh spectrum showed that fits with the Fh/HFO spectrum were slightly better for the 6 samples formed at $(P/Fe)_{init}$ of 0.05, 0.1, 0.2, 0.6, 0.75 and 1.0, whereas the Fh reference returned slightly better fit results for the 3 samples formed at $(P/Fe)_{init}$ of 0.3, 0.4, and 0.5 with the highest ferrihydrite-type precipitate fractions. Comparison of the LCF-derived fractions obtained with the Fh/HFO and the Fh reference spectra (Table EA2, Fig. EA7) showed that the pcLp*a-fraction did not depend on the choice of ferrihydrite-type reference spectrum, but that fits with the Fh/HFO reference spectrum returned on average 32% (relative) higher fractions for the ferrihydrite-type precipitate than fits with the Fh reference and correspondingly lower FeP* fractions.

Table EA2. LCF results for aged precipitates formed at $(P/Fe)_{init}$ from 0.05 to 1.0, with either the HFO, Fh/HFO or Fh reference spectrum as proxy for the ferrihydrite-type precipitate fraction.

Fh-type reference	$(P/Fe)_{init, th}$	FeP*	Fh-type	pcLp*a	Sum	NSSR (x1000)	$(NSSR/NSSR_{HFO})-1$
HFO	0.05	--	0.16	0.84	1.02	1.35	
	0.10	--	0.15	0.85	1.03	1.62	
	0.20	--	0.38	0.62	1.02	1.60	
	0.30	--	0.66	0.34	1.03	8.07	
	0.40	--	0.89	0.11	1.03	12.8	
	0.50	--	0.94	0.06	1.03	13.7	
	0.60	0.17	0.70	0.13	1.04	5.66	
	0.75	0.46	0.42	0.12	1.04	2.99	
	1.00	0.87	0.13	--	1.01	0.70	
Fh/HFO	0.05	--	0.17	0.83	1.03	1.29	-4%
	0.10	--	0.15	0.85	1.04	1.57	-3%
	0.20	--	0.39	0.61	1.04	1.45	-9%
	0.30	--	0.67	0.33	1.08	3.88	-52%
	0.40	--	0.90	0.10	1.09	4.22	-67%
	0.50	0.15	0.77	0.07	1.04	6.84	-50%
	0.60	0.26	0.60	0.14	1.05	2.58	-54%
	0.75	0.54	0.33	0.13	1.04	3.07	3%
	1.00	0.90	0.10	--	1.01	0.74	6%
Fh	0.05	--	0.17	0.83	1.03	1.43	6%
	0.10	--	0.15	0.85	1.04	1.70	5%
	0.20	0.12	0.23	0.65	1.01	1.48	-8%
	0.30	0.14	0.50	0.36	1.05	3.51	-57%
	0.40	0.21	0.65	0.14	1.05	3.69	-71%
	0.50	0.31	0.59	0.10	1.01	6.72	-51%
	0.60	0.39	0.45	0.16	1.02	2.88	-49%
	0.75	0.62	0.23	0.15	1.02	3.39	13%
	1.00	0.93	0.07	--	1.01	0.84	20%

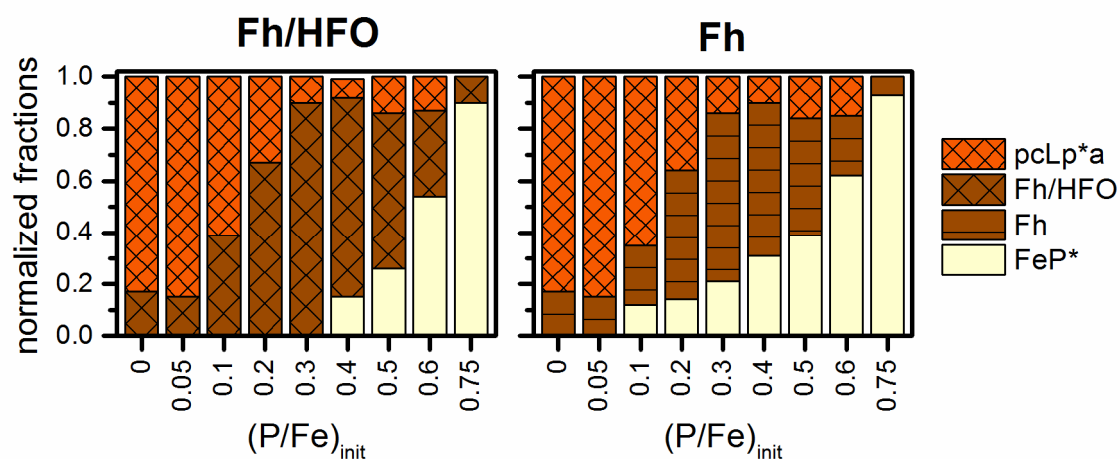


Fig. EA7. LCF results with Fh/HFO or Fh to represent the ferrihydrite-type precipitate fraction for aged precipitates formed at $(P/Fe)_{init}$ of 0.05 to 1.0 in the Na electrolyte. The LCF results are given in Table EA2.

Overview of references used for LCF analysis

Table EA3. Overview of references used for LCF analysis of the different series.

Series	Reference					
	FeP*	CaFeP*	lowCaFeP*	Fh/HFO	Fh-Si*	pcLp*a
Na	x			x		x
Ca		x		x		x
Mg	x			x		x
low Ca			x	x		x
Na+Si	x				x	
Ca+Si		x			x	

Fe K-edge EXAFS LCF results and precipitate P/Fe ratios

In Table EA4, the effective initial and the precipitate P/Fe ratios (from ICP-MS analysis) and Fe K-edge EXAFS LCF results are listed for all precipitates. Absolute and relative uncertainties for individual fractions derived from LCF are summarized in Table EA5 (average, standard deviation, 90th percentile and maximum of absolute and relative uncertainty for each fraction).

Table EA4. Initial dissolved and final precipitate P/Fe ratios and Fe K-edge EXAFS LCF results for aged precipitates. All sample and reconstructed LCF spectra are shown in Fig. EA8, the LCF results are graphically presented in Fig. 3. For each background electrolyte, only the references considered for LCF are tabulated. LCF-derived fractions normalized to a sum of 1 are listed together with the effective sum of the fitted fractions. NSSR represents the normalized sum of squared residuals ($NSSR = \sum (data_i - fit_i)^2 / \sum (data_i)^2$). Further details on the LCF analysis are given in section 2.3. Fit uncertainties are summarized in Table EA5. Underlined values were used for linear regression analysis (section EA6, Table EA7). The LCF results for fresh precipitates are provided in the electronic annex of Senn et al. (2015).

Series	P/Fe ratios		LCF results				
	(P/Fe) _{init}	(P/Fe) _{ppt}	FeP*	Fh/HFO	pcLp*a	Sum	NSSR (x1000)
Na	0.00	0.00	--	--	1.00	1.00	0.70
	0.04	0.02	--	0.17	0.83	1.03	1.29
	0.09	0.02	--	0.15	0.85	1.04	1.57
	0.19	<u>0.05</u>	--	<u>0.39</u>	<u>0.61</u>	1.04	1.45
	0.31	<u>0.11</u>	--	<u>0.67</u>	<u>0.33</u>	1.08	3.88
	0.41	<u>0.15</u>	--	<u>0.90</u>	<u>0.10</u>	1.09	4.22
	0.51	<u>0.19</u>	<u>0.15</u>	<u>0.77</u>	<u>0.07</u>	1.04	6.84
	0.60	<u>0.24</u>	<u>0.26</u>	<u>0.60</u>	<u>0.14</u>	1.05	2.58
	0.75	<u>0.36</u>	<u>0.54</u>	<u>0.33</u>	<u>0.13</u>	1.04	3.07
	0.99	0.56	0.90	0.10	--	1.01	0.74
	1.46	0.61	0.92	0.08	--	1.01	2.28
	1.91	0.68	0.91	0.09	--	1.02	0.90
Series	(P/Fe) _{init}	(P/Fe) _{ppt}	CaFeP*	Fh/HFO	pcLp*a	Sum	NSSR (x1000)
Ca	0.00	0.00	--	0.00	1.00	1.03	3.07
	0.04	0.03	--	0.10	0.90	1.01	2.04
	0.08	0.05	--	0.16	0.84	0.98	2.44
	0.18	<u>0.12</u>	--	<u>0.39</u>	<u>0.61</u>	1.03	1.64
	0.29	<u>0.23</u>	<u>0.19</u>	<u>0.35</u>	<u>0.46</u>	1.04	2.04
	0.39	<u>0.33</u>	<u>0.32</u>	<u>0.37</u>	<u>0.31</u>	1.03	1.20
	0.49	<u>0.45</u>	<u>0.52</u>	<u>0.26</u>	<u>0.22</u>	1.01	1.42
	0.58	<u>0.54</u>	<u>0.57</u>	<u>0.31</u>	<u>0.12</u>	1.02	1.01
	0.74	<u>0.71</u>	<u>0.83</u>	<u>0.15</u>	<u>0.02</u>	1.01	3.21
	0.95	0.89	1.00	--	--	1.00	2.23
	1.29	1.26	1.00	--	--	1.00	3.90
	1.96	1.92	1.00	--	--	0.99	3.48

Table EA4. continued.

Series	P/Fe ratios		LCF results				
	(P/Fe) _{init}	(P/Fe) _{ppt}	FeP*	Fh/HFO	pcLp*a	Sum	NSSR (x1000)
Mg	0.00	0.00	--	--	1.00	0.96	1.88
	0.05	0.03	--	0.21	0.79	1.01	1.87
	0.10	0.05	--	0.27	0.73	1.01	1.99
	0.20	<u>0.10</u>	<u>0.09</u>	<u>0.36</u>	<u>0.55</u>	1.01	1.87
	0.30	<u>0.16</u>	<u>0.14</u>	<u>0.56</u>	<u>0.31</u>	1.04	2.25
	0.42	<u>0.27</u>	<u>0.28</u>	<u>0.53</u>	<u>0.20</u>	1.01	1.95
	0.50	<u>0.35</u>	<u>0.40</u>	<u>0.55</u>	<u>0.05</u>	1.04	2.05
	0.59	<u>0.46</u>	<u>0.58</u>	<u>0.42</u>	--	1.02	1.39
	0.73	<u>0.59</u>	<u>0.74</u>	<u>0.26</u>	--	0.99	2.59
	0.97	0.69	0.85	0.15	--	1.00	2.31
	1.44	0.76	0.89	0.11	--	0.97	2.13
	1.91	0.79	0.89	0.11	--	1.01	1.96
Series	(P/Fe) _{init}	(P/Fe) _{ppt}	lowCaFeP*	Fh/HFO	pcLp*a	Sum	NSSR (x1000)
low Ca	0.00	0.00	--	--	1.00	1.01	1.22
	0.05	0.03	--	0.11	0.89	1.00	2.02
	0.10	0.05	--	0.17	0.83	0.98	2.19
	0.20	<u>0.09</u>	--	<u>0.42</u>	<u>0.58</u>	1.03	2.78
	0.31	<u>0.18</u>	<u>0.16</u>	<u>0.48</u>	<u>0.37</u>	1.05	2.41
	0.42	<u>0.33</u>	<u>0.41</u>	<u>0.31</u>	<u>0.29</u>	0.99	2.22
	0.48	<u>0.40</u>	<u>0.53</u>	<u>0.34</u>	<u>0.13</u>	1.03	1.53
	0.60	<u>0.49</u>	<u>0.68</u>	<u>0.20</u>	<u>0.12</u>	1.02	5.07
	0.73	<u>0.66</u>	<u>0.87</u>	<u>0.13</u>	--	1.01	3.87
	0.98	0.74	1.00	--	--	1.01	3.74
	1.41	0.80	1.00	--	--	1.01	2.32
	1.88	0.87	1.00	--	--	1.02	3.09

Table EA4. continued.

Series	P/Fe ratios		LCF results			
	(P/Fe) _{init}	(P/Fe) _{ppt}	FeP*	Fh-Si*	Sum	NSSR (x1000)
Na+Si	0.00	0.00	--	1.00	0.99	3.92
	0.04	0.03	--	1.00	0.99	2.65
	0.08	0.05	--	1.00	0.99	3.60
	0.18	<u>0.08</u>	--	<u>1.00</u>	0.99	4.09
	0.30	<u>0.17</u>	<u>0.17</u>	<u>0.83</u>	1.01	3.33
	0.40	<u>0.27</u>	<u>0.39</u>	<u>0.61</u>	0.97	4.34
	0.50	<u>0.41</u>	<u>0.75</u>	<u>0.25</u>	0.98	2.67
	0.57	<u>0.45</u>	<u>0.78</u>	<u>0.22</u>	0.96	1.47
	0.70	<u>0.51</u>	<u>0.90</u>	<u>0.10</u>	0.98	1.51
	0.94	0.57	0.90	0.10	1.00	1.08
	1.43	0.64	1.00	--	0.99	2.56
	1.84	0.68	1.00	--	0.99	1.50
Series	(P/Fe) _{init}	(P/Fe) _{ppt}	CaFeP*	Fh-Si*	Sum	NSSR (x1000)
Ca+Si	0.00	0.00	0.14	0.86	0.99	6.29
	0.03	0.03	0.10	0.90	0.98	2.63
	0.08	0.08	0.25	0.75	0.97	6.60
	0.18	<u>0.17</u>	<u>0.31</u>	<u>0.69</u>	0.95	7.46
	0.30	<u>0.28</u>	<u>0.38</u>	<u>0.62</u>	1.00	2.85
	0.38	<u>0.36</u>	<u>0.54</u>	<u>0.46</u>	0.96	4.13
	0.48	<u>0.46</u>	<u>0.64</u>	<u>0.36</u>	0.98	4.20
	0.57	<u>0.55</u>	<u>0.67</u>	<u>0.33</u>	0.98	2.12
	0.69	<u>0.67</u>	<u>1.00</u>	--	0.96	4.18
	0.92	0.88	1.00	--	0.99	2.28
	1.37	1.33	1.00	--	1.00	4.03
	1.82	1.78	1.00	--	1.01	2.49

Table EA5. Absolute and relative statistical uncertainties of fractions obtained from LCF analysis. For each reference spectrum, the average, standard deviation, 90th percentile (90-PCTL) and maximal uncertainty of the fitted fractions are provided (taking all samples/spectra into account where the reference was considered). The values were derived from the "best" fits. The n -component fit with the lowest NSSR was considered to be the "best" fit if no $n+1$ -component fit returned a more than 10% (relative) lower NSSR.

	FeP*		CaFeP*		lowCaFeP*		Fh/HFO		Fh-Si*		pcLp*a	
	abs	rel	Abs	rel	abs	rel	abs	rel	abs	rel	abs	rel
average	0.01	4%	0.01	4%	0.01	2%	0.01	5%	0.02	5%	0.00	2%
std. dev.	0.00	4%	0.01	5%	0.01	3%	0.01	5%	0.01	4%	0.00	4%
90-PCTL	0.02	9%	0.02	10%	0.02	5%	0.02	14%	0.03	9%	0.01	4%
maximum	0.02	15%	0.03	17%	0.02	8%	0.03	17%	0.03	15%	0.01	21%

Fe K-edge EXAFS spectra of aged precipitates and reconstructed LCF spectra

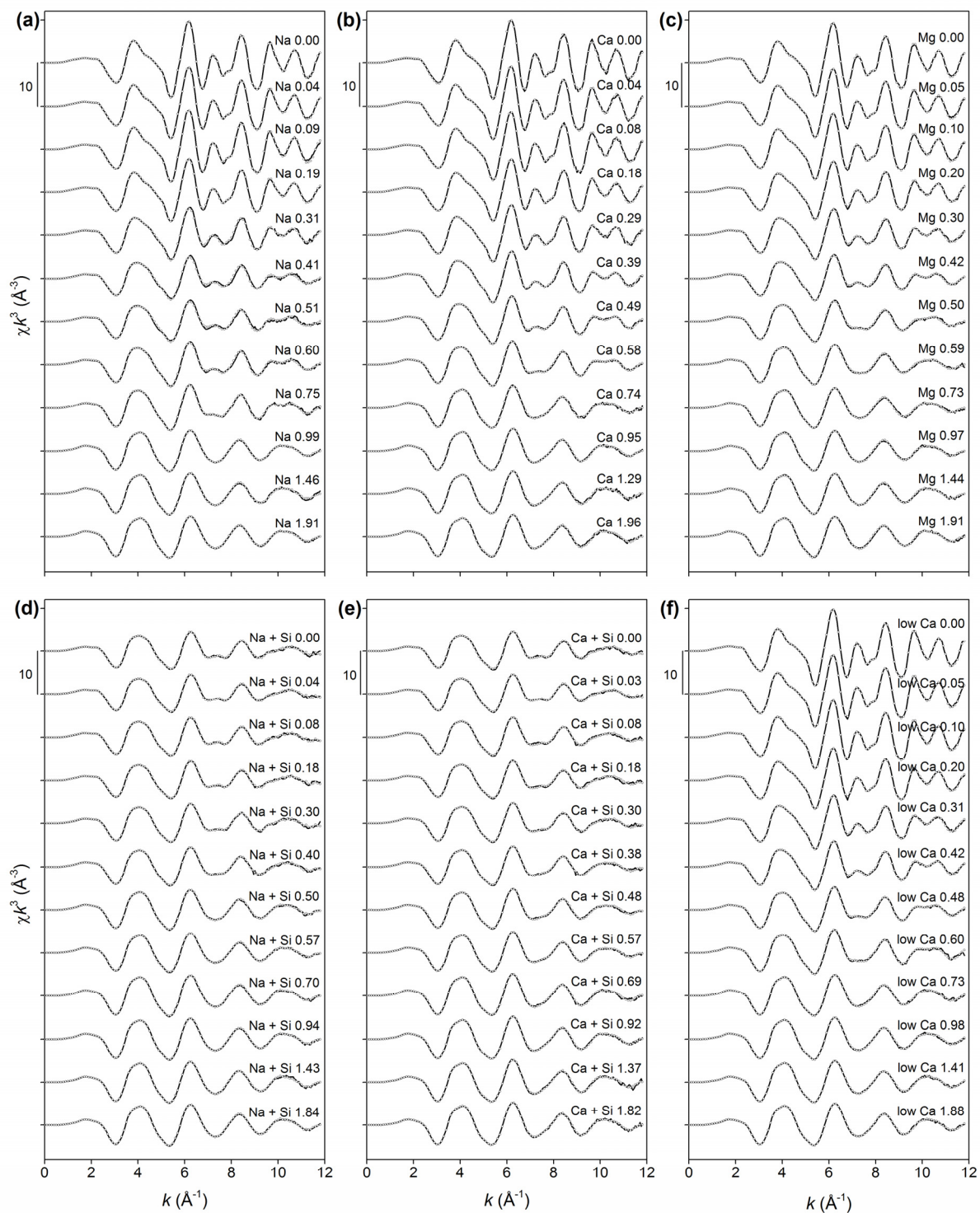


Fig. EA8. Fe K-edge EXAFS spectra (solid lines) and reconstructed LCF spectra (open circles) of aged Fe(III)-precipitates formed in Na, Ca, Mg, low Ca, Na+Si, and Ca+Si electrolytes (a-f). Numbers at the right of the spectra indicate the background electrolyte and the molar initial dissolved P/Fe ratio ($(P/Fe)_{\text{init}}$). Sample details and LCF results are listed in Table EA4.

Fe K-edge EXAFS analysis of precipitates formed in absence of arsenate

Table EA6. Results of the LCF analysis of the spectra of aged Fe(III)-precipitates formed in the absence of 0.014 arsenate/Fe in the phosphate-free Na, Mg, low Ca and Ca electrolytes. The reported fractions were normalized to unity. The NSSR represents the normalized sum of the squared residuals of the fits. The reconstructed fits are shown in Fig. EA9. The fitted fractions are also shown in Fig. 4 in the main manuscript.

	Series	pcLp*a	Goe	Sum	NSSR (x1000)
fresh	Na	0.93	0.07	0.98	1.68
	Mg	0.93	0.07	0.98	1.68
	low Ca	0.95	0.05	0.99	1.55
	Ca	1.00	0.00	1.01	2.14
aged	Na	0.22	0.78	0.99	3.9
	Mg	0.77	0.23	0.95	3.4
	low Ca	0.42	0.58	0.98	3.4
	Ca	0.95	0.05	1.02	2.0

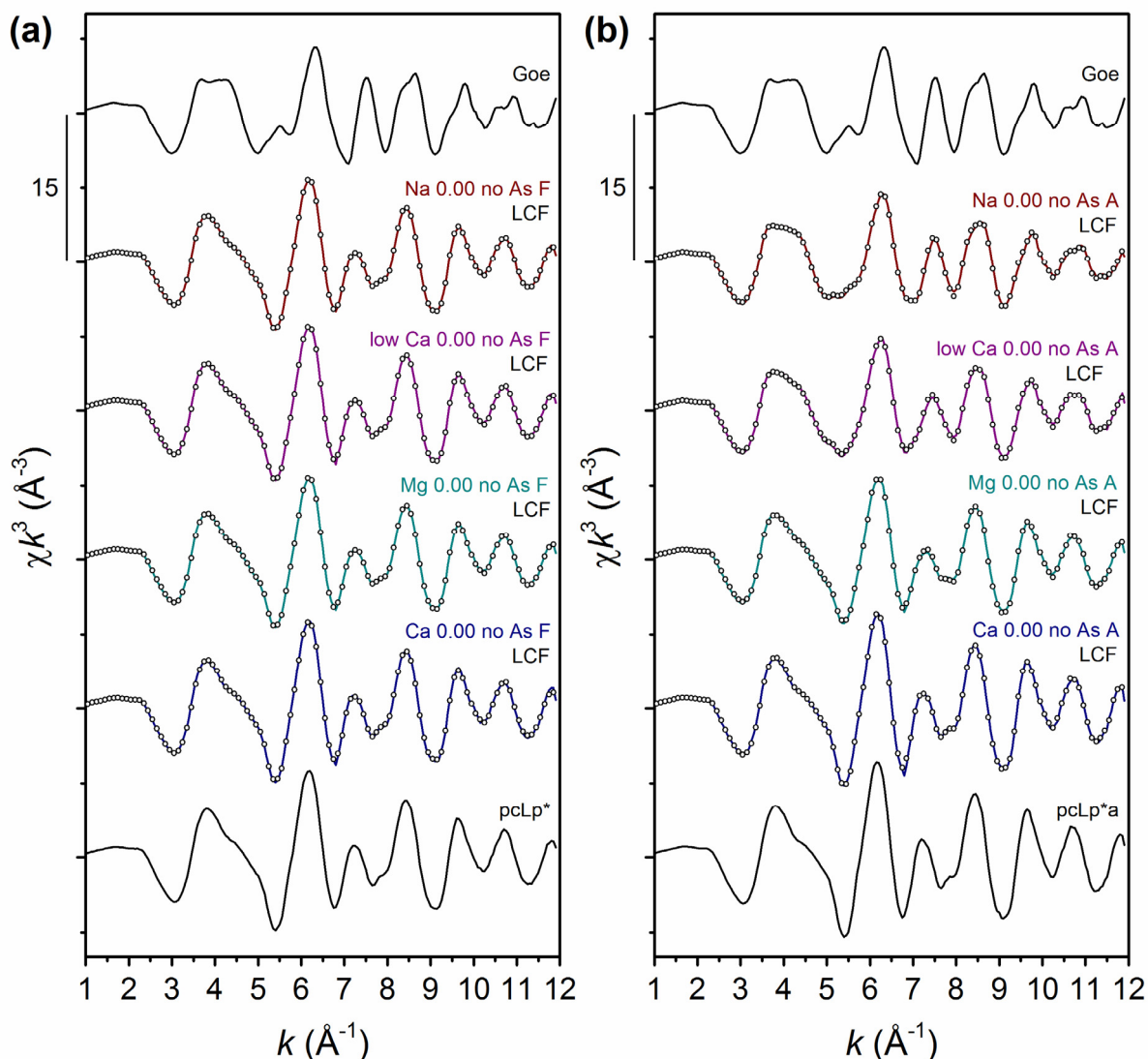


Fig. EA9. Fe K-edge EXAFS spectra (solid lines) and reconstructed LCF spectra (open circles) of fresh (a) and aged (b) Fe(III)-precipitates formed in absence of arsenate in Na, low Ca, Mg and Ca electrolytes compared to the reference spectrum of goethite (Goe) and the endmember spectrum of fresh and aged poorly crystalline lepidocrocite (pcLp* and pcLp*a), respectively. The LCF results are listed in Table EA6, the fractions are also shown Fig. 4 in the main manuscript.

EA4. X-ray diffraction data

For the analysis of selected precipitates by X-ray diffraction (XRD), the respective experiments in Na and Ca background electrolyte were performed in larger solution volumes (1000 mL), otherwise following the described protocol in the main manuscript.

For XRD analysis, 30 mg of dried precipitate were suspended in ethanol, transferred onto 27-mm diameter low-background Si-slides and allowed to dry. XRD patterns were recorded from 5 to 95° 2- θ with a step-size of 0.017° and a measurement time of 6 h per sample using Co K α radiation (X'Pert Powder diffractometer with X'Celerator detector, PANalytical, Almelo, The Netherlands). The XRD patterns shown in Fig. EA10 were scaled to a unity increase from the lowest to the highest measured intensity.

Using the Scherrer equation, coherent scattering domain sizes of 28 nm (Na 0.00 Å) and 30 nm (Ca 0.00 Å) were estimated from the 200 peaks at ~16.0 2-theta.

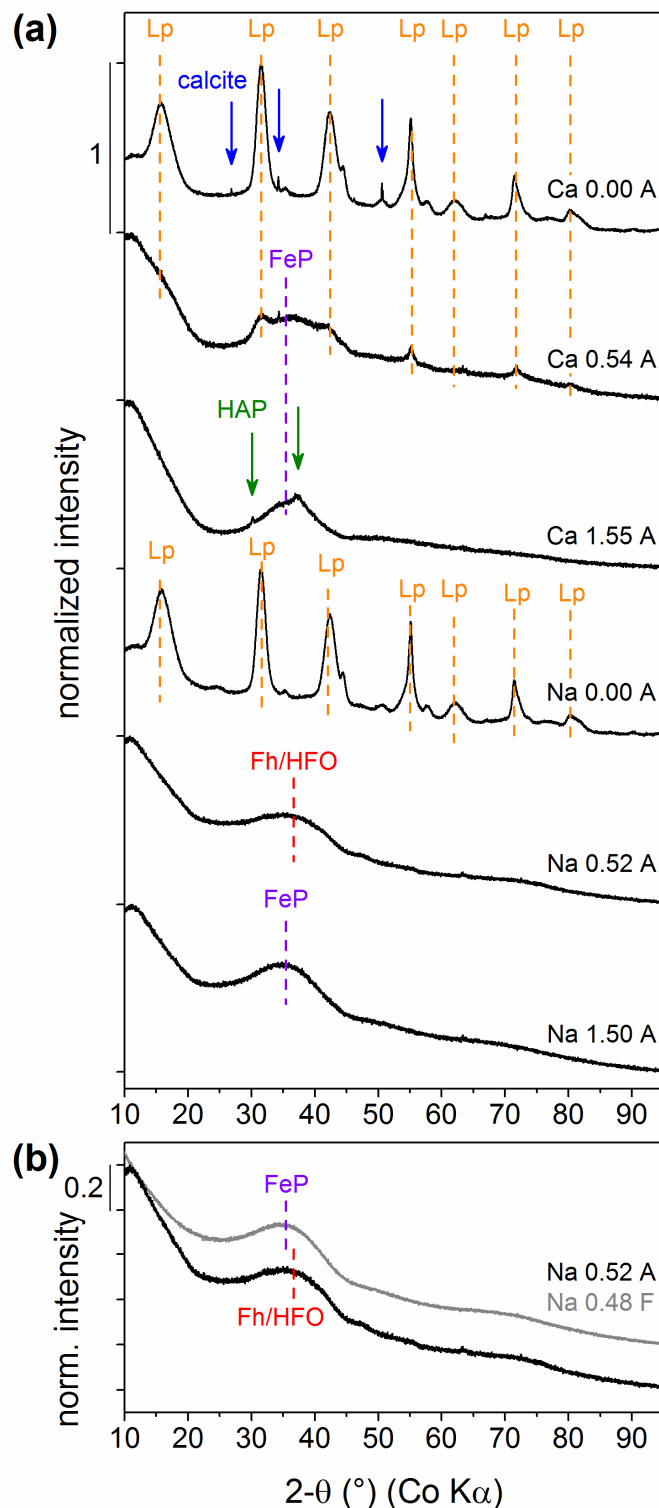


Fig. EA10. (a) X-ray diffraction spectra of aged Fe(III)-precipitates formed in Na and Ca electrolyte at selected $(P/Fe)_{init}$ (black solid lines). Dashed vertical lines correspond to dominant peaks of lepidocrocite (Lp), ferrihydrite-type Fe(III)-phosphate transformation product (Fh/HFO) and amorphous Fe(III)-phosphate (FeP). Arrows indicate the peaks of calcite (blue, Ca 0.00 A) and HAP (green, Ca 1.55 A). The intensities were normalized to cover a range of unity. (b) Comparison of the spectrum of the aged precipitate at $(P/Fe)_{init} \sim 0.5$ with the spectrum of the respective fresh precipitate.

EA5. Additional scanning TEM images

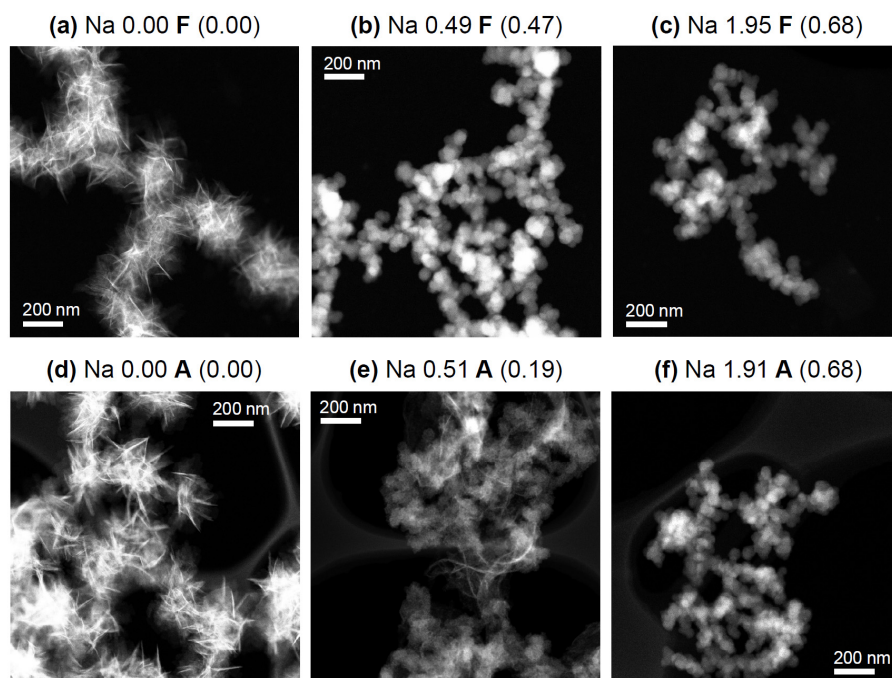


Fig. EA11. High-angle annular dark field (HAADF) STEM images indicating the mass-thickness contrast of selected fresh (a–c) and aged (d–f) Fe(III)-precipitates formed in Na electrolyte at different $(P/Fe)_{init}$ ($(P/Fe)_{ppt}$ in parentheses). The corresponding secondary electron (SE) images are shown in Fig. 5.

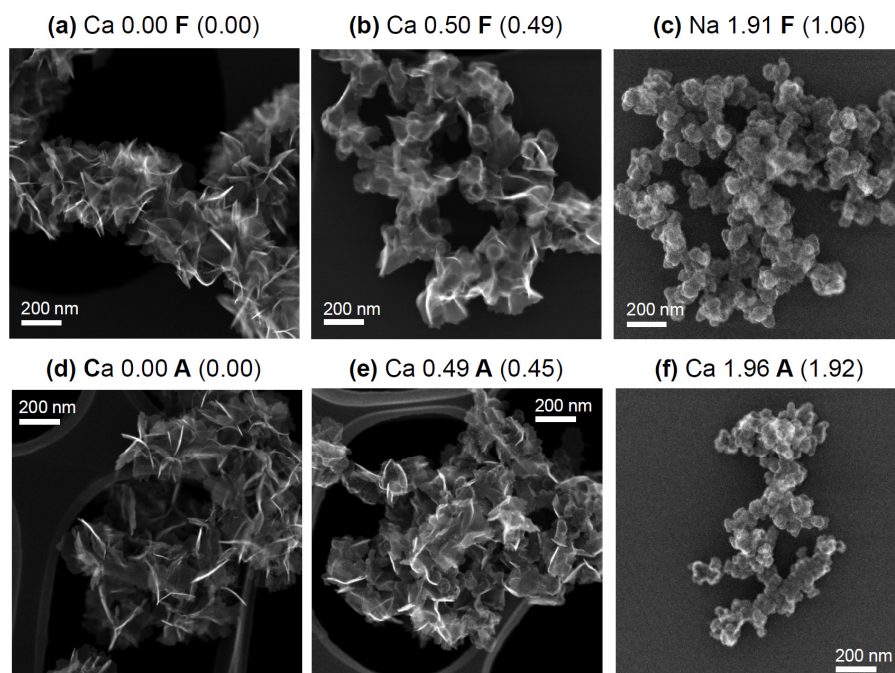


Fig. EA12. Secondary electron (SE) STEM images indicating the morphology of selected fresh (a–c) and aged (d–f) Fe(III)-precipitates formed in Ca electrolyte at different $(P/Fe)_{init}$ ($(P/Fe)_{ppt}$ in parentheses).

EA6. Molar (P/Fe)_{ppt} ratios of precipitate fractions from linear regressions

Table EA7. Molar (P/Fe)_{ppt} ratios of Fe(III)-phosphate- and ferrihydrite-type precipitates calculated from multiple linear regressions of (P/Fe)_{ppt} over LCF-derived fractions.

	Fe(III)-phosphate	Ferrihydrite
Series	(P/Fe) _{(lowCa)FeP*}	(P/Fe) _{Fh/HFO, Fh-Si*}
Na	0.56 (0.02)	0.15 (0.01)
Mg	0.74 (0.02)	0.10 (0.02)
low Ca	0.70 (0.02)	0.16 (0.04)
Na+Si	0.55 (0.01)	0.09 (0.01)

The molar (P/Fe)_{ppt} of the FeP* or lowCaFeP* and Fh/HFO or Fh-Si* fractions derived from LCF analysis were calculated by multiple linear regressions based on the (P/Fe)_{ppt} of precipitates formed at (P/Fe)_{init} from ~0.2 to ~0.75 and the respective LCF results (listed in Table EA4). During optimization, the P/Fe ratios were constrained to positive values. For lepidocrocite, P/Fe ratios of 0 were obtained if it was included in the regression analysis. Analogous P/Fe ratios for fresh precipitates have been published in Senn et al. (2015).

EA7. Saturation indices of Ca-phosphates in low Ca and Ca electrolytes

Table EA8. Saturation indices (SI) for hydroxyapatite (HAP), tricalciumphosphate (TCP), octacalciumphosphate (OCP) and brushite in the aged low Ca and Ca electrolyte suspensions at (P/Fe)_{init} of 1.5 and 0.3, based on measured pH, dissolved Ca and phosphate. The thermodynamic calculations were performed using PHREEQC with the Minteq V4 database using the CO₂ partial pressure to set the pH to the measured value. For OCP, the SI in parentheses was calculated using an alternative solubility product from (Tung et al., 1988).

	low Ca suspensions		Ca suspensions	
(P/Fe)_{init}	1.5	0.3	1.5	0.3
pH	8.1	7.9	7.9	8.0
Ca (mM)	0.26	0.40	3.6	3.0
phosphate (mM)	0.29	0.05	0.03	0.02
HAP	9.0	7.0	10.5	10.0
TCP	1.3	0.0	2.1	1.7
OCP (Tung et al., 1988)	-0.6 (0.7)	-2.5 (-1.1)	0.1 (1.4)	-0.5 (0.8)
Brushite	-1.0	-1.5	-1.0	-1.2

EA8. References

- Isaure, M., Laboudigue, A., Manceau, A., Sarret, G., Tiefert, C., Trocellier, P., Lambelle, G., Hazeman, J., Chateignier, D. (2002). Quantitative Zn speciation in a contaminated dredged sediment by μ -PIXE, μ -SXRF, EXAFS spectroscopy and principal component analysis. *Geochimica et Cosmochimica Acta* **66**, 1549-1567.
- Manceau, A., Marcus, M.A., Tamura, N. (2002) Quantitative speciation of heavy metals in soils and sediments by synchrotron X-ray techniques, in: Fenter, P.A., Rivers, M.L., Sturchio, N.C., Sutton, S.R. (Eds.), *Reviews in Mineralogy and Geochemistry*. Mineralogical Society of America, Washington, pp. 341-428.
- Marcus, M.A., Macdowell, A.A., Celestre, R.S., Manceau, A., Miller, T., Padmore, H.A., Sublett, R.E. (2004). Beamline 10.3.2 at ALS: a hard X-ray microprobe for environmental and materials sciences. *Journal of Synchrotron Radiation* **11**, 239-247.
- Senn, A.-C., Kaegi, R., Hug, S.J., Hering, J.G., Mangold, S., Voegelin, A. (2015). Composition and structure of Fe(III)-precipitates formed by Fe(II) oxidation in water at near-neutral pH: Interdependent effects of phosphate, silicate and Ca. *Geochimica et Cosmochimica Acta* **162**, 220-246.
- Tung, M.S., Eidelma, N., Sieck, B., Brown, W.E. (1988). Octacalcium phosphate solubility product from 4 to 37 °C. *Journal of Research of the National Bureau of Standards*. **93**, 613-624.